Optogenetic and chemical genetic tools for rapid repositioning of vimentin intermediate filaments

Milena Pasolli [1]*, Joyce C. M. Meiring [1]*, James P. Conboy [2],
Gijsje H. Koenderink [2] and Anna Akhmanova [1]

[1] Cell Biology, Neurobiology and Biophysics, Department of Biology, Faculty of Science, Utrecht University, Padualaan, Utrecht, 3584 CS, The Netherlands.

[2] Department of Bionanoscience, Kavli Institute of Nanoscience Delft, Delft University of Technology, 2629 HZ Delft, The Netherlands.

* Equal contribution

Corresponding author: Anna Akhmanova, a.akhmanova@uu.nl

Abstract

Intermediate filaments (IFs) are a key component of the cytoskeleton, essential for regulating cell mechanics, maintaining nuclear integrity, organelle positioning, and modulating cell signaling. Current insights into IF function primarily come from studies using long-term perturbations, such as protein depletion or mutation. Here, we present tools that allow rapid manipulation of vimentin IFs in the whole cytoplasm or within specific subcellular regions by inducibly coupling them to microtubule motors, either pharmacologically or using light. Rapid perinuclear clustering of vimentin had no major immediate effects on the actin or microtubule organization, cell spreading, or focal adhesion number, but reduced cell stiffness. Mitochondria and endoplasmic reticulum sheets were reorganized due to vimentin clustering, whereas lysosomes were only briefly displaced and rapidly regained their normal distribution. Keratin moved along with vimentin in some cell lines but remained intact in others. Our tools help to study the immediate and local effects of vimentin perturbation and identify direct links of vimentin to other cellular structures.

Introduction

Intermediate filaments (IFs), along with actin and microtubules, are among the three major cytoskeletal systems in mammalian cells (Herrmann and Aebi, 2004). Unlike microtubules and actin, IFs lack polarity, exhibit much slower dynamics and are extremely resilient and elastic (Etienne-Manneville, 2018; Herrmann et al., 2007). Among them, vimentin, a type III IF protein, is a prominent component of cells of mesenchymal origin (Mendez et al., 2010). Recent structural work indicated that vimentin forms a helical structure of 40 α-helices organized into five protofibrils that are connected by the vimentin tails, with the head domains located in the lumen (Eibauer et al., 2024). Vimentin IFs surround the nucleus and spread throughout the cytoplasm, a distribution facilitated by microtubule-based motors (Hookway et al., 2015; Robert et al., 2019). Additionally, due to interactions with actin filaments, the vimentin network is subject to actin-driven retrograde flow (Leduc and Etienne-Manneville, 2017).

Vimentin plays an important role in many cellular processes, such as cell mechanics and control of cell stiffness (Guo et al., 2013; Pogoda and Janmey, 2023), maintenance of cell shape, cell-substrate adhesion and cell migration (Bhattacharya et al., 2009; Cheng and Eriksson, 2017; Eckes et al., 2000; Eckes et al., 1998; Venu et al., 2022). Furthermore, vimentin participates in templating and stabilizing microtubule networks (Gan et al., 2016; Schaedel et al., 2021) and is involved in the positioning and anchorage of organelles such as mitochondria (Nekrasova et al., 2011), endo-lysosomes, and endoplasmic reticulum (ER) (Cremer et al., 2023). Finally, vimentin plays a role in signaling and gene regulation (Paulin et al., 2022).

The cellular functions of vimentin have been primarily studied using knockout and knockdown approaches (Bhattacharya et al., 2009; Colucci-Guyon et al., 1994; Eckes et al., 2000; Kural et al., 2007; Mendez et al., 2014; Mohanasundaram et al., 2022; Ostrowska-Podhorodecka et al., 2022). While these studies have provided insights into the consequences of vimentin loss, they could not distinguish the direct and immediate interactions and interdependencies between vimentin and other cellular structures from the long-term effects caused by the absence of vimentin and the ensuing compensatory cellular changes, including alterations in gene expression.

Treatments perturbing vimentin organization have also been used to study its function (Ridge et al., 2016). For example, overexpression of defective gigaxonin, an E3 ligase adaptor, induces dense perinuclear aggregation of vimentin filaments (Bomont, 2016; Mahammad et al., 2013). Similarly, withaferin A, a natural product with anti-tumor and anti-angiogenesis properties, reorganizes vimentin into perinuclear aggregates but lacks specificity, impacting not only other IFs but also actin and microtubules (Bargagna-Mohan et al., 2007; Grin et al., 2012). Another pharmacological agent, simvastatin, was shown to induce bundling and collapse of vimentin filaments (Lavenus et al., 2020; Trogden et al., 2018), but its use as a tool is complicated by additional effects, such as its impact on cholesterol synthesis. Furthermore, microinjected mimetic peptides were used to disrupt filament assembly and rapidly

reorganize the vimentin network (Goldman et al., 1996; Helfand et al., 2011). While these peptides act quickly—causing changes within minutes—they often disrupt other cytoskeletal components, leading to cellular alterations like rounding and blebbing (Goldman et al., 1996). Their specificity is further limited as they are derived from conserved IF regions (Strelkov et al., 2002), potentially affecting other IF networks. Additionally, microinjection requires specialized expertise and equipment, reducing accessibility and reproducibility. Altogether, this underlines the need for more precise tools to reorganize vimentin IFs and directly observe their interactions and effects on other cellular structures.

In this study, we developed a robust method to rapidly relocalize vimentin filaments, either locally or globally, by recruiting to them microtubule-based motors using either chemical or light-induced heterodimerization. This allowed us to observe vimentin interactions and interdependencies with other cellular structures and their dynamic behavior on a time scale of 15-60 minutes, which is too short to alter gene expression. We found that clustering of vimentin in the cell center by microtubule minus-end-directed kinesins had only mild effects on the actin and microtubule cytoskeleton, and no major impact on cell spreading and focal adhesion number but strongly reduced cell stiffness. The keratin-8 network was not affected by vimentin displacement in HeLa cells but was co-clustered with vimentin in U2OS and COS-7 cell lines, supporting the cell-type-specific nature of IF organization. ER sheets and mitochondria were relocalized together with vimentin, confirming their direct interactions. In contrast, lysosomes were only mildly affected, and their normal distribution was rapidly restored. Our method enables acute and controlled studies of the role of vimentin in cytoskeletal crosstalk and organelle positioning and dynamics, revealing short-term effects and steady-state alterations.

Results

Chemically induced repositioning of vimentin to microtubule plus or minus ends

To induce rapid repositioning of vimentin IFs, we used a chemically inducible heterodimerization system to recruit to vimentin microtubule-based motors, as described previously for membrane organelles (Kapitein et al., 2010). In cells with a radial microtubule organization, recruitment of minus-end-directed motors concentrates cargoes near the cell nucleus, whereas plus-end-directed motors disperse cargoes towards the cell periphery (Kapitein et al., 2010).

The system we used was based on inducible binding of two protein domains, FRB and FKBP, upon the addition of a rapamycin analog (rapalog AP21967, also known as A/C heterodimerizer) (Clackson et al., 1998; Pollock et al., 2000). We fused the FKBP domain and a fluorescent marker, mCherry, to the C-terminus of vimentin (Figure 1A, B), as this is the preferred tagging site for avoiding aggregation and ensuring proper filament assembly (Herrmann et al., 1996; Usman et al., 2022). The FRB domain was fused to a kinesin motor to induce controlled movement. To trigger minus-end-directed transport towards the microtubule-organizing center (MTOC) (Figure 1C), we employed the motor domain (amino acids 861–1321) of a moss kinesin-14 type VI kinesin-14b from the moss *Physcomitrella patens* (hereafter referred to as ppKin14)(Jonsson et al., 2015). The motor was tetramerized through a fusion with the leucine zipper domain of GCN4 (Nijenhuis et al., 2020), and tagged with a BFP or GFP fluorescent marker for visualization (Chen et al., 2022). This motor was selected because by itself, it does not perturb endogenous transport in mammalian cells but can efficiently pull cargoes when artificially coupled to them (Nijenhuis et al., 2020). For plus-end-directed transport towards the cell periphery (Figure 1C), we used a hemagglutinin (HA)-tagged dimeric motor domain fragment of the neuronal kinesin-1 KIF5A (amino acids 1–560) (Figure 1A, B). This motor was chosen for its demonstrated efficiency in pulling the highly interconnected and abundant ER network, which spans the entire cell (Özkan et al., 2021). Flexible glycine-serine (GS) linkers were inserted between the fusion protein domains to ensure proper protein folding and functionality.

To test these constructs, we have transiently transfected them in COS-7 cells, fixed the cells after treatment with ethanol solvent with or without rapalog and stained them for total vimentin, and in the case of the plus-end-directed motor, also for the HA tag (Figure 1D-E). The mCherry-tagged vimentin strongly colocalized with total vimentin (Figure 1D-E, Figure S1A), and the signal and the distribution of the latter appeared largely unperturbed in the absence of rapalog, though the fraction of the cell area occupied by vimentin was slightly larger in transfected cells than in untransfected control cells (Figure 1F). To assess the efficacy of motor recruitment, we conducted a 5-minute treatment with and without rapalog, followed by super-resolution imaging of ppKin14 and KIF5A motors enhanced by antibody staining (Figure S1B-C). The results showed that, in the absence of rapalog, the motors did not associate with vimentin filaments: ppKin14 appeared diffuse, whereas KIF5A aligned with

130 filaments that likely represented a stable microtubule subset, as published previously (Cai et
131 al., 2009; Dunn et al., 2008; Reed et al., 2006). Upon rapalog addition, both motors densely
132 populated vimentin filaments (Figure S1B-C). Treatment with rapalog for 1 hour had no effect
133 on vimentin distribution in untransfected cells; however, in transfected cells the vimentin
134 network collapsed completely (Figure 1D-F). In ppKin14 transfected cells, a single vimentin
135 cluster was formed at the cell center, as expected. Surprisingly, the outcome in cells
136 expressing KIF5A was quite similar, with a major vimentin cluster in the cell center and some
137 additional, smaller clusters in the peripheral cytoplasm (Figure 1E, F). This conclusion was
138 confirmed by analyzing the fraction of cell area occupied by vimentin, using cells with similar,
139 moderate construct expression levels, which represented ~50% of the total transfected cell
140 population (Figure 1F-I). In the remaining 50% of the cells, the construct expression was either
141 too high, causing vimentin pulling even without rapalog, or insufficient to allow vimentin
142 repositioning. Similar results were obtained in U2OS cells (Figure S1D-E), indicating that these
143 effects were not cell line-specific.

144 To observe vimentin relocalization in real time, we performed live cell imaging before and
145 after rapalog addition (Figure 1J, L). Vimentin repositioning towards microtubule minus ends
146 with ppKin14 occurred rapidly, with strong vimentin clustering visible already within 10 min,
147 likely due to the dense nature of the vimentin network in the cell center (Figure 1J, Video 1).
148 The effect of KIF5A was slower (clustering visible within 20 min) and resulted in a pronounced
149 tug-of-war (Video 2 and 3), leading to the formation of vimentin clusters at microtubule
150 crossroads at the cell periphery in addition to vimentin accumulation in the cell center (Figure
151 1L). After an hour of rapalog treatment, cells were fixed and stained for total vimentin,
152 confirming its repositioning (Figure 1K, M). Taken together, our findings demonstrate that the
153 rapalog-induced kinesin recruitment can trigger rapid vimentin displacement from most of
154 the cytoplasm, with the minus-end-directed ppKin14 organizing a single centrally positioned
155 cluster, and the plus-end-directed KIF5A forming additional smaller clusters at the cell
156 periphery.

157 **Light-induced vimentin repositioning**

158 We next modified the system by substituting the FKBP and FRB domains for the components
159 of the improved Light Induced Dimerizer (iLID) system (Guntas et al., 2015). This system
160 consists of an optimized LOV2 domain derived from *Avena sativa* conjugated to the bacterial
161 peptide SsrA (iLID), and the SsrA-interacting domain SspB. In the dark state, the SsrA in iLID is
162 sterically blocked by LOV2, but upon LOV2 activation with blue light, SsrA becomes available
163 for binding by SspB (Guntas et al., 2015). We fused the iLID to the two kinesin motors and
164 linked the mCherry-tagged C-terminus of vimentin to $SspB_{micro}$ (Figure 2A-C). The Vim-mCh-
165 SspB successfully integrated into the endogenous vimentin network (Figure 2D). Upon a 5-
166 min blue light illumination, U2OS cells transiently transfected with iLID-GFP-GCN4-ppKin14
167 and Vim-mCh-SspB exhibited motor recruitment to vimentin filaments (Figure S2A), similar to
168 the FRB-FKBP system (Figure S1B). Longer blue light illumination was expected to induce

169 vimentin relocalization, which was indeed observed. After 45 minutes of whole-cell blue light
170 illumination, followed by fixation and staining for total vimentin, relocalization was confirmed
171 (Figure 2E, F). To assess the performance of the tool, we analyzed cells with comparable
172 expression levels, evaluated by fluorescence intensity of the tags of the transfected constructs
173 (Figure 2G, H). Amongst all transfected cells, ~40% were in the optimal range, ~40% were
174 overexpressing the constructs too much, resulting in vimentin clustering without blue light
175 illumination, and ~20% had too low expression, insufficient to trigger vimentin clustering in
176 lit conditions. Within the optimized expression range, clustering of vimentin in the cell center
177 was observed only in transfected cells, and only upon blue light illumination (Figure 2E, F).
178 This treatment had no effect on the cell area, indicating that vimentin clustering had no major
179 effect on cell spreading (Figure 2I).

180 The advantage of light-induced heterodimerization is that it can also be used for subcellular
181 manipulations. Indeed, by using local illumination with blue light, we could cause vimentin
182 retraction in a part of the cell, without affecting vimentin distribution in the rest of the
183 cytoplasm (Figure 2J, K). Subsequent fixation and staining for vimentin confirmed that
184 endogenous vimentin was also locally displaced along with the tagged vimentin (Figure 2L).

185 Another advantage of the iLID-SspB system compared to the rapalog-induced
186 heterodimerization is that it is reversible. In order to evaluate reversibility, we first exposed
187 transfected U2OS cells to 30 minutes of intermittent blue light, which resulted in vimentin
188 clustering in the center of the cell, and then continued imaging the tagged vimentin without
189 blue light to allow cells to recover (Figure 2M, Video 4). Cells required between 2.5 and 4
190 hours to restore vimentin distribution (Figure 2M, N), likely through a combination of diffusion
191 and active transport by the kinesin-1 motor, which transports vimentin filaments toward the
192 cell periphery (Gyoeva and Gelfand, 1991; Robert et al., 2019). While some cells exhibited
193 complete recovery, others regained only 40-70% of the initial vimentin density at the
194 periphery (Figure 2N). This variability could not be explained by differences in expression
195 levels (Figure S2B), but could be related to differences in the cell cycle phase or in the degree
196 of vimentin compaction near the MTOC, potentially caused by crosslinking proteins trapped
197 within the dense mesh (Petitjean et al., 2024; Wiche and Winter, 2011).

198 Finally, we also tested optogenetic vimentin repositioning in combination with the KIF5A-iLID
199 fusion by whole cell illumination and found that it worked similarly to KIF5A-FRB: vimentin
200 formed some peripheral clusters, with a significant part of the filaments accumulating in the
201 cell center (Figure S2C-E). Repositioning vimentin with a minus-end-directed kinesin proved
202 more effective than with a plus-end-directed motor, likely due to the dense organization of
203 the vimentin network in the perinuclear region.

204 **Vimentin clustering has little immediate effects on microtubules, actin, and focal adhesions**

205 Considering that microtubules and vimentin can reciprocally affect each other (Gan et al.,
206 2016; Prahlad et al., 1998; Schaedel et al., 2021), we next investigated whether vimentin

clustering affects microtubule organization. To this end, COS-7 cells were co-transfected with Vim-mCh-FKBP and either FRB-BFP-GCN4-ppKin14 or HA-KIF5A-FRB, with non-transfected cells serving as controls (Figure 3A, B). After one hour treatment with or without rapalog, the cells were fixed and stained for tyrosinated tubulin, a marker of dynamic microtubules. The overall microtubule intensity did not differ between transfected and non-transfected cells, nor between rapalog-treated and untreated conditions (Figure 3C). However, we noted that the microtubule network appeared slightly more disorganized in transfected cells, likely due to the overexpression of vimentin and motor proteins. This disorganization was not significantly different after pulling vimentin in either direction, as quantified by the ratio of non-radial to radial microtubules (Figure 3D).

Next, we examined whether stable microtubules would be affected by vimentin pulling. Given that COS-7 cells displayed variable levels of stable microtubules, as indicated by acetylated tubulin staining (data not shown), we performed these experiments in U2OS cells, which have much more consistent levels of stable microtubules. Cells were fixed after one hour of treatment with or without rapalog. Cells co-expressing Vim-mCh-FKBP and FRB-BFP-GCN4-ppKin14 exhibited similar levels of acetylated tubulin compared to non-transfected cells, regardless of the treatment condition (Figure 3E, G). However, cells co-expressing Vim-mCh-FKBP with HA-KIF5A-FRB showed significantly reduced acetylated tubulin levels even without rapalog addition (Figure 3F, G), and the expression of HA-KIF5A-FRB alone was sufficient to cause this effect (Figure S3A, B). This is consistent with a recent study showing that overexpression of kinesin-1 KIF5B fragment 1-560 reduces the number of stable, acetylated microtubules (Andreu-Carbó et al., 2024), which are the preferred tracks for this motor in cells (Cai et al., 2009; Dunn et al., 2008; Reed et al., 2006). Due to this strong effect of the KIF5A motor on stable microtubules, we decided to focus on minus-end-directed pulling in subsequent experiments to avoid indirect effects of perturbing stable microtubules on the studied structures.

We next examined the effects of vimentin clustering on actin stress fibers and focal adhesions, structures that have been reported to be linked to vimentin IFs (Bhattacharya et al., 2009; Esue et al., 2006; Jiu et al., 2015; Mendez et al., 2010; Tsuruta and Jones, 2003; Venu et al., 2022). One hour after initiating rapalog-induced vimentin network relocalization by ppKin14, COS-7 cells were fixed and stained for total vimentin, F-actin, and the focal adhesion marker paxillin. Despite strong vimentin clustering, we observed no changes in the cell area, the appearance of F-actin structures, or the number of focal adhesions (Figure 4A-C). We repeated these experiments in U2OS cells, which have more prominent stress fibers and focal adhesions, but again observed no significant changes after vimentin repositioning (Figure 4D-F). This is consistent with the results of light-induced vimentin repositioning described above, where no effect on cell area was observed (Figure 2I). Our findings indicate that the clearance of vimentin from the cytoplasm and its clustering in the cell center do not have major short-term effects on microtubules, actin, or the ability of cells to adhere to substrate and spread.

246 **Co-dependency of keratin-8 and vimentin localization is cell-type dependent**

247 We next examined the impact of rapalog-inducible vimentin clustering on keratin IFs using
248 COS-7, U2OS, and HeLa cells. All three cell lines showed endogenous expression of keratin-8,
249 with the highest expression observed in HeLa cells (Figure S4A). In COS-7 cells, the keratin-8
250 and vimentin networks exhibited strong colocalization in the cell center, with keratin being
251 more abundant than vimentin at the cell periphery (Figure S4B). Super-resolution imaging
252 showed that the two proteins could be detected in the same filaments (Figure 5A, B, Figure
253 S4B, C). Overexpression of vimentin in COS-7 cells resulted in a more fragmented keratin-8
254 network and reduced its abundance at the cell periphery (Figure 5A). However, co-
255 localization between keratin-8 and vimentin in transfected cells persisted, even following
256 vimentin clustering (Figure 5A, B). Similarly, U2OS cells showed high vimentin-keratin-8
257 colocalization, with both proteins sometimes incorporated into the same filaments, although
258 keratin-8 appeared more sparse (Figure 5C, D, Figure S4D, E). Also in U2OS cells, vimentin
259 pulling efficiently cleared keratin-8 from the cytoplasm (Figure 5C, D). These findings indicate
260 a strong interdependence between the two IF types in COS-7 and U2OS cells.

261 In HeLa cells, both networks were dense around the nucleus, but the keratin-8 network also
262 formed connections to the plasma membrane via desmosomes, as described previously
263 (Figure 5E, Figure S4F, G) (Jones and Goldman, 1985; Nishizawa et al., 2005; Schwarz et al.,
264 2015). Unlike COS-7 and U2OS cells, vimentin and keratin-8 networks in HeLa cells appeared
265 much more distinct and displayed a lower colocalization coefficient (Figure 5F), although
266 some filaments containing both IF types were also observed (Figure 5E, Figure S4F, G).
267 Vimentin clustering did not affect the distribution of keratin-8 in HeLa cells, as reflected by a
268 significant reduction in colocalization (Figure 5E, F). These results imply significant differences
269 in the organization of vimentin and keratin-8 networks between cell types.

270 **Vimentin relocalization to the MTOC reduces cell stiffness**

271 Previous studies have demonstrated that cells lacking vimentin exhibit reduced stiffness and
272 increased deformability (Mendez et al., 2014; Messica et al., 2017; Shaebani et al., 2022).
273 Building on these findings, we aimed to investigate the effect of vimentin reorganization on
274 cellular mechanical properties, with a particular focus on cell stiffness. To explore this, we
275 used rapalog induced vimentin reorganization in U2OS cells (Figure 6A) and measured cell
276 stiffness using a spherical nanoindenter to determine the Young's modulus (Figure S5).
277 Indentations were performed at three locations within the perinuclear region (Figure 6B).
278 Cells in which vimentin was pulled toward the cell center exhibited a reduction in Young's
279 modulus of more than 60% compared to control cells (Figure 6C). This significant decrease in
280 cell stiffness indicates that vimentin reorganization makes U2OS cells softer and more
281 deformable, aligning with previous findings from vimentin knockout studies (Mendez et al.,
282 2014; Messica et al., 2017; Shaebani et al., 2022).

283 **Vimentin pulling drives ER reorganization and reveals redundancy of ER-vimentin linkers**

284 Next, we investigated the effect of vimentin repositioning on intracellular membranes.
285 Vimentin and the ER display a significant degree of co-localization, especially in the
286 perinuclear area where ER sheets are present, as well as at the more peripherally located ER
287 matrices (Cremer et al., 2023; Lynch et al., 2013; Nixon-Abell et al., 2016) (Figure 7A, B). At
288 the cell periphery, ER intensity decreases, coinciding with the polygonal ER network and a
289 sparser vimentin distribution (Figure 7A).

290 Using the optogenetic tool, we observed that ER sheets and matrices but not tubules were
291 pulled along with vimentin, confirming their previously described direct connections (Cremer
292 et al., 2023) (black arrows, Figure 7C; Video 5). Most of the vimentin and ER repositioning
293 occurred within approximately 10 minutes (Figure 7C, D, Video 5). While initially this resulted
294 in a sparser tubular ER network at the cell periphery, over time, the network became denser,
295 with smaller polygonal structures. This effect could also be observed in the ratio of perinuclear
296 to peripheral intensity, where a subset of ER initially follows vimentin to the perinuclear region
297 but then redistributes again towards cell periphery (Figure 7D). It should be noted that while
298 photobleaching of the ER channel was negligible, there was a 40% reduction in total Vim-mCh-
299 SspB intensity over the course of the experiment (Figure 7E).

300 A similar pattern for ER reorganization was seen in fixed COS-7 cells using the rapalog-based
301 tool to sequester vimentin (Figure 7F). After one hour of rapalog-induced vimentin clustering,
302 we observed two distinct phenotypes: in some cells, the ER remained sparse and mostly
303 confined to the perinuclear area; in other cells, ER reorganized, forming smaller polygons that
304 extended toward the periphery (Figure 7F).

305 Next, we investigated the effect of vimentin pulling in the absence of RNF26, a recently
306 described linker between ER sheets and vimentin (Cremer et al., 2023). We used U2OS wild
307 type (WT) and RNF26 knockout cells and performed localized light-induced vimentin
308 relocalization inside a region of interest at the cell periphery (blue dashed box, Figure 8A, B,
309 Video 6 and 7). Surprisingly, even in the absence of RNF26, vimentin pulling resulted in
310 concomitant retraction of the ER sheets and matrices (Figure 8B; Video 7). This was also
311 demonstrated by the reduction in fluorescence intensity of the ER marker inside the region of
312 interest accompanying the drop in vimentin intensity (Figure 8C). This implies the existence of
313 additional linkers between the ER network and the vimentin cytoskeleton.

314 **Vimentin-mediated mitochondrial re-localization persists after pulling, whereas lysosomes**
315 **rapidly recover**

316 We next investigated the effects of vimentin repositioning on other organelles. U2OS cells
317 were used, because in these cells, organelles are distributed throughout the cell, whereas in
318 COS-7 cells most organelles are strongly clustered in the perinuclear region, and their
319 relocalization with vimentin would be less obvious. Local vimentin pulling revealed that the
320 clearance of vimentin led to a strong redistribution of mitochondria (Figure 9A, Video 8).
321 Mitochondria remained co-clustered with vimentin also during longer (one hour) treatment

322 periods, as observed in fixed cells after using the rapalog tool (Figure 9B). The fraction of
323 mitochondria at the cell periphery (defined as the cell area outside the perinuclear region,
324 which was empirically defined as a circle with a radius of 13.82 µm) was reduced in rapalog-
325 treated transfected cells compared to untreated transfected cells (Figure 9C).

326 In contrast, lysosomes demonstrated a different behavior. In optogenetic experiments,
327 lysosomes were initially pulled along with vimentin, but quickly dissociated from the vimentin
328 cluster and returned to the cell periphery (Figure 9D, Video 9). This was confirmed by the long-
329 term (one hour) rapalog treatment and analysis of fixed cells, which showed no significant
330 changes in lysosome distribution between treated and untreated cells (Figure 9E). The
331 lysosome fraction at the cell periphery (outside the perinuclear region) remained the same,
332 ~40% (Figure 9F). These data indicate that vimentin IFs are not a dominant factor in the steady-
333 state distribution of lysosomes, and their transient displacement could be caused by their
334 entrapment in the vimentin mesh or presence of the membrane contact sites with other
335 organelles, such as the ER or mitochondria.

Discussion

In this study, we have introduced a rapid chemical and optogenetic approach to reposition the vimentin network, which can be precisely controlled in time and space. In cells with a radial microtubule organization and significant perinuclear clustering of vimentin, a minus-end-directed kinesin could rapidly (within ~10 min) clear the cytoplasm of the majority of vimentin filaments, without strongly perturbing either microtubules or the actin cytoskeleton. Also a plus-end directed kinesin-1-derived tool disrupted the vimentin network, but it turned out to be less useful, because it was slower and led to formation of both peripheral and perinuclear vimentin clusters. This was likely because vimentin forms a very dense perinuclear cage that is difficult to pull apart; moreover, some of the preferred tracks of kinesin-1, stable microtubules, are positioned with their plus ends facing the cell periphery (Chen et al., 2022) and could target vimentin towards the nucleus.

The optogenetic approach for clustering vimentin was reversible, suggesting that pulling did not damage vimentin filaments. The recovery was, however, incomplete in some cells, possibly due to differences in the cell cycle stage, or because the forces generated by kinesin-1 (Robert et al., 2019) may be insufficient to fully restore vimentin's original distribution. Furthermore, vimentin clustering might cause increased crosslinking via the tail domains (Aufderhorst-Roberts and Koenderink, 2019; Lin et al., 2010), or perhaps by proteins like plectin becoming trapped within the filament mesh (Foisner et al., 1988; Wiche and Baker, 1982; Wiche and Winter, 2011).

Our findings confirmed established functions of the vimentin network and provided new insights into its interactions with other cellular structures. Unlike previous approaches to perturb vimentin that often affected the organization of other cytoskeletal components such as microtubules, actin stress fibers and focal adhesions (De Pascalis et al., 2018; Grin et al., 2012; Havel et al., 2014; Saldanha et al., 2023; Swoger et al., 2022), our chemical and optogenetic manipulation of vimentin did not have a marked short-term effect on the appearance of these structures in the studied cell types in 2D cultures in glass. However, we have not investigated the effects of vimentin clustering on the dynamics of focal adhesions or the actin cytoskeleton. Rapidly migrating cells, such as fibroblasts, characterized by faster adhesion turnover rates (Gupton and Waterman-Storer, 2006; Mavrakis and Juanes, 2023) and larger focal adhesions (Kim and Wirtz, 2013) may react differently to vimentin perturbation. Given that our tools do not cause cell toxicity on a short time scale and can be applied locally, they could be used to study mechanistic details that were previously inaccessible, such as the local impact vimentin on cell polarity and adhesion dynamics (Venu et al., 2022). Furthermore, it will now be possible to distinguish direct effects of vimentin contacts with other cytoskeletal structures from the changes in signaling or gene expression induced by vimentin loss. Finally, since previous work has suggested that cells migrating on soft substrates are more sensitive to the loss of vimentin (Swoger et al., 2022), it would be interesting to test whether the same phenotypes can be reproduced with inducible vimentin clustering.

375 We identified cell-type-specific differences in the interactions between vimentin and keratin.
376 In COS-7 and U2OS cells, where the two IF types are co-expressed (termed hybrid cell states
377 by Sha et al., 2019) but keratin levels are relatively low, super-resolution microscopy indicated
378 that keratin and vimentin can co-assemble into the same filaments, and keratin-8 was pulled
379 along with vimentin. In HeLa cells, where keratin levels are higher, co-assembly seemed to be
380 less frequent, and vimentin clustering did not impact the keratin network. Colocalization of
381 vimentin and keratin in certain epithelial cells has been detected previously (Robert et al.,
382 2019; Velez-delValle et al., 2016) but has not received much attention, and it deserves further
383 investigation.

384 Vimentin relocalization led to a strong reduction in stiffness of U2OS cells, consistent with
385 findings from vimentin knockout cells (Mendez et al., 2014; Messica et al., 2017; Shaebani et
386 al., 2022). Since we did not observe any changes in the actin or microtubule cytoskeleton in
387 the time frame of the experiment but did find that keratin-8 co-clusters with vimentin in
388 analyzed cells, we conclude that IFs by themselves make a major contribution to cell rigidity.

389 We also examined the relationship between vimentin and the ER, building on previous
390 findings (Cremer et al., 2023; Lynch et al., 2013). Colocalization of the vimentin and ER
391 networks, particularly ER matrices (Nixon-Abell et al., 2016) and sheets during acute vimentin
392 displacement confirmed their physical interaction. Notably, even in the absence of vimentin-
393 ER linker, RNF26, ER displacement together with vimentin was still observed, implying the
394 existence of other linkers. Potential candidates for this function are nesprins, such as nesprin-
395 3, which can connect to vimentin through plectin (Ketema et al., 2013; Nery et al., 2008).
396 While these proteins are mostly concentrated in the nuclear envelope by binding to the SUN
397 domain proteins at the inner nuclear membrane (Kim et al., 2015), they are transmembrane
398 proteins that could be present in other ER compartments.

399 In addition to ER, other organelles were affected by vimentin pulling. Mitochondria moved
400 together and remained co-clustered with vimentin, consistent with previous observations that
401 vimentin influences mitochondrial positioning (Nekrasova et al., 2011). Meanwhile, lysosomes
402 showed only transient interactions with vimentin, as a fraction of lysosomes co-clustered with
403 vimentin during pulling but rapidly regained their original distribution. This suggests a much
404 weaker interaction, probably mediated by the contacts with the ER network (Kilpatrick et al.,
405 2013; Özkan et al., 2021) or by entrapment in the vimentin mesh.

406 In summary, our vimentin-pulling tool is versatile and can be applied across various cell types.
407 Future optimizations, such as tagging and pulling endogenous vimentin using a knock-in
408 approach or generation of clonal stable cell lines, could help minimize side effects associated
409 with vimentin and motor protein overexpression, and improve the reproducibility of
410 reversible pulling assays. This tool can shed light on cytoskeletal dependencies, cell protrusion
411 and migration, and distinguish the immediate effects of vimentin reorganization on cell
412 architecture from the long-term impact on signaling pathways and gene expression.

413 **Materials & Methods**

Chemicals, peptides, and recombinant proteins	Company	Catalog number
SiR-tubulin	Spirochrome	SC014
Janelia Fluor 646 HaloTag Ligand	Promega	GA1120
FuGENE 6	Promega	E2692
Pen/strep	Gibco	15140-122
Gibson Assembly Master Mix	Thermo Fisher	A46629
ProLong™ Glass Antifade Mountant	Thermo Fisher Scientific/Life Tech	P36984
16% PFA Methanol-free	Fisher Emergo	28908
Aqueous Glutaraldehyde EM Grade, 10%	Electron Microscopy Sciences	16110
A/C Heterodimerizer (rapalog)	Takara	AP21967
A/C Heterodimerizer (rapalog)	Bio Connect	635056

414

Cell lines		
HeLa Kyoto	Narumiya S., Kyoto University	CVCL_1922
COS-7	ATCC	CVCL_0224
U2OS	ATCC	CVCL_0042
U2OS RNF26 KO	Berlin I., Leiden University Medical Center (Cremer et al., 2023)	

415

Recombinant DNA	
FRB-BFP-GCN4-ppKin14	Chen et al. 2022
FRB-GFP-GCN4-ppKin14	Chen et al. 2022
HA-KIF5A-FRB	This paper
Vim-mCh-FKBP	This paper
iLID-GFP-GCN4-ppKin14	This paper
KIF5A-mVenus-iLID	This paper
Vim-mCh-SspB	This paper
Halo-KDEL	Meiring et al. 2022
Halo-mitoTag	This paper
LAMP1-Halo	Meiring et al. 2022

416 **Software-plugins**

FIJI	ImageJ	https://imagej.net/software/fiji/downloads
ComDet plugin	Fiji	https://github.com/ekatrukha/ComDet
Radiality map plugin	Fiji	https://github.com/UU-cellbiology/radialitymap

Radius plugin	Fiji	https://gist.github.com/ekatrukha/105553627f1bee01367faae153bfe5c0
MtrackJ	Smal et al. (2008)	N/A
Sigma Plot	Systat Software Inc.	7
Excel	Microsoft	Office16
Prism	Graphpad	10.1.1(323)
MetaMorph	Molecular Devices	7.10.2.240
Dataviewer	Optics11	2

417

418 **Cell culture and transfections**

419 COS-7, HeLa, U2OS wild-type, and RNF26 knockout cells were cultured in Dulbecco's Modified
420 Eagle Medium (DMEM; Sigma), supplemented with 10% fetal calf serum (FCS), 100 U/ml
421 penicillin, and 100 µg/ml streptomycin (1% Pen Strep; Sigma). Cells were maintained at 37 °C
422 in a humidified atmosphere with 5% CO2 and were regularly tested for mycoplasma
423 contamination. For immunostaining, cells were plated on 18 mm coverslips, while 25 mm
424 coverslips or gridded dishes (Lonza) were used for live cell imaging. Gridded dishes were used
425 if cells needed to be first imaged live and then found back after fixing and staining. Transient
426 transfections were performed using the Fugene 6 transfection reagent, following the
427 manufacturer's protocol. For optogenetic construct transfections in 6 well plates, 2 µg Vim-
428 mCh-SspB and 500 ng iLID-GFP-GCN4-ppKin14 or 200 ng KIF5A-mVenus-iLID was used per
429 well; for 12 well plates the quantity was halved. For chemical pulling experiments in 6-well
430 plates, each well was transfected with 500 ng of Vim-mCh-FKBP and either 250 ng of FRB-BFP-
431 GCN4-ppKin14 or HA-KIF5A-FRB. In 12-well plates, the quantities were also halved. Cells were
432 subjected to rapalog treatments, live cell imaging, or fixation one day post-transfection.

433 **Drug treatment**

434 For rapalog-inducible dimerization experiments, cells were plated on 18 mm cover glasses
435 and co-transfected the following day with Vim-mCh-FKBP and either FRB-BFP-GCN4-ppKin14/
436 FRB-GFP-GCN4-ppKin14or HA-KIF5A-FRB constructs. Twenty-four hours post-transfection,
437 cells were treated with 400 nM rapalog (AP21967 A/C heterodimerizer, Takara) for 5min or
438 one hour.

439 **Plasmids and cloning**

440 The Vim-mCh-FKBP construct was generated using PCR-based cloning combined with Gibson
441 assembly. The mCherry-N1 construct served as the backbone, with vimentin amplified from
442 human cDNA encoding isoform 1 of vimentin (corresponding to CCDS7120, 466 amino acids),
443 and the FKBP domain amplified from the FKBP-mCherry-CAMSAP2 plasmid (Chen et al., 2022).
444 GS linkers were included between protein segments. The FRB-BFP-GCN4-ppKin14 and FRB-

445 GFP-GCN4-ppKin14 were described previously (Chen et al., 2022). In order to make Vim-mCh-
446 SspB, Vimentin was first amplified from from human cDNA encoding isoform 1 (corresponding
447 to CCDS7120, 466 amino acids) and cloned in to the KIF1A(1-365)-GFP-SspB plasmid (Addgene
448 #174629) (Nijenhuis et al., 2020) replacing KIF1A, cut out using AscI and XbaI restriction sites,
449 by Gibson assembly, next the GFP was replaced by the mCherry from SspB-mCh-p60 (Addgene
450 #190168) (Meiring et al., 2022) by restriction enzyme cloning using XbaI and NheI restriction
451 sites. The iLID-GFP-GCN4-ppKin14 was generated from SspB-GFP-GCN4-ppKin14 (Addgene
452 #174640)(Nijenhuis et al., 2020) by restriction enzyme cloning using AscI and XbaI restriction
453 sites to replace the SspB with the iLID from iLID-mCl3-Tau0N4R (Meiring et al., 2022). The
454 KIF5A-mVenus-iLID was cloned by first substituting the SspB in KIF1A(1-365)-Venus-SspB
455 (Addgene #174635) (Nijenhuis et al., 2020) for an iLID from EB3N-VVDfast-mCl3-iLID (Addgene
456 #190165) (Meiring et al., 2022) by restriction enzyme cloning using NheI and NdeI restriction
457 sides, and subsequently replacing the KIF1A with KIF5A amplified from 3xHA-KIF5A-FRB using
458 AscI and XbaI restriction sites and Gibson assembly. The Halo-Mitotag was made by cutting
459 out the Rab6a from Halo-Rab6a (Addgene #190171) (Meiring et al., 2022) using KpnI and
460 BamHI and inserting the C-terminal tail of the actA protein as a mitochondrial targeting
461 sequence (Zhu et al., 1996) 5'-
462 TTAATTCTTGCAATGTTAGCTATTGGCGTGTTCTCTTTAGGGGCGTTTATCAAAATTATTCAATTAAGAAA
463 AAATAAT -3' by Gibson assembly. Halo-KDEL and LAMP1-Halo were previously described in
464 (Meiring et al., 2022). 3xHA-KIF5A-FRB was kindly provided by Ginny Farías (Utrecht
465 University, The Netherlands). mCherry-N1, KIF1A-GFP-SspB, KIF1A(1-365)-mVenus-SspB, (1-
466 365)-GFP-SspB and SspB-GFP-GCN4-ppKin14 were gifts from Lukas Kapitein (Utrecht
467 University, The Netherlands). All constructs were confirmed by DNA sequencing.

468 **Antibodies, immunofluorescence staining, and Western blotting**

469 Different fixation methods were employed depending on the target protein for
470 immunofluorescence experiments. For vimentin, microtubules, and keratin-8, cells were fixed
471 on ice in ice-cold methanol for 5-15 minutes. For calnexin staining, cells were fixed with 0.1%
472 glutaraldehyde (GA), 4% paraformaldehyde (PFA), and 4% sucrose pre-warmed at 37°C for 10
473 minutes at room temperature. Cytochrome C, Lamtor4, phalloidin, and paxillin staining were
474 performed on cells fixed in 4% PFA in PBS for 15 minutes at room temperature. Post-fixation,
475 cells were washed thrice with PBS and, unless methanol fixed, permeabilized with 0.2% Triton
476 X-100 in PBS for 2.5 minutes. Following another washing step with PBS, cells fixed with GA
477 were quenched with 100 mM sodium borohydride in PBS three times, 5 minutes each. After
478 another PBS washing step, cells were blocked in 2% BSA in PBS for an hour at room
479 temperature. The incubation of the primary and secondary antibodies was done at room
480 temperature for an hour, with the antibodies diluted in 2% BSA in PBS. Phalloidin conjugated
481 to 647 fluorophore was added with the secondary antibodies. Between the primary and
482 secondary antibody incubations, there was a washing step with 0.05% Tween-20 in PBS. After
483 the last wash, coverslips were mounted with ProLong Gold mounting media.

484 The following primary antibodies were used in this study:

485

Primary antibodies Antibody	**Host**	**Company**	**Catalog number**	**Dilution** IF /WB
Actin c4	Mouse	Sigma-Aldrich/Merck	MAB1501	-/1:1000
Calnexin	Rabbit	Abcam	22595	1:250
Cytochrome C	Mouse	BD Pharmingen	556432	1:200
Cytokeratin-8 (K8/KRT8)	Rat	DSHB, TROMA-I	AB_531826	1:12/ 1:100
GFP	Mouse	Sigma-Aldrich	11814460001	1:200
HA	Rat	Covance		1:200
HA	Mouse	Covance		1:200
LAMTOR4 (D6A4V)	Rabbit	Cell Signalling	12284	1:200
Paxillin	Mouse	BD Biosciences	610619	1:200
Tubulin-acetylated	Mouse	Sigma-Aldrich	T7451-200UL	1:200
Tubulin-acetylated (Lys40)	Rabbit	Bioke	5335S	1:500
Tubulin-alpha YL1/2 (tyrosinated)	Rat	Pierce/Thermo	MA1-80017	1:400
Vimentin	Chicken	Abcam	ab24525	1:200
Vimentin	Rabbit	Abcam	ab92547	1:400
Vimentin V9	Mouse	Sigma-Aldrich	V6630	1:200/ 1:1000

486

487 Alexa Fluor −405,–488, –594 and −647 conjugated highly cross-preabsorbed goat antibodies
488 against rabbit, rat, and mouse IgG were used as secondary antibodies. Anti-rabbit and anti-rat
489 secondary antibodies were from Thermo Fischer, anti-mouse secondary antibodies were from
490 Jackson ImmunoResearch. Secondary antibodies were all used at a dilution of 1:200/250.

491 For Western blotting, cells were harvested at 90–100% confluency from a 10 cm dish. Lysis
492 was performed using RIPA buffer, supplemented with protease and phosphatase inhibitors
493 (Roche). Proteins were separated on 10% polyacrylamide gels and transferred onto 0.45 µm
494 nitrocellulose membranes (Sigma-Aldrich). Membrane blocking was performed in 2% BSA in
495 PBS for 30 minutes at room temperature. The membrane was initially exposed to primary
496 antibodies overnight at 4°C, then washed three times with 0.05% Tween-20 in PBS. Next,
497 IRDye 680LT and 800CW anti-mouse and anti-rat secondary antibodies (LI-COR Biosciences)
498 diluted 1:1,000 in 2% BSA in PBS were added, and the membrane was incubated for one hour
499 at room temperature before being washed again with 0.05% Tween-20 in PBS. Finally,
500 membranes were imaged on an Odyssey CLx infrared imaging system (Image Studio version
501 5.2.5, LI-COR Biosciences).

502 **HaloTag labelling**

503 HaloTag dye JF646 (Promega) was diluted in DMSO to 200 µM, aliquoted and stored at -20 °C.
504 Aliquoted HaloTag dye was diluted 1:10,000 in prewarmed cell media, vortexed for 5 s and
505 incubated with cells overnight.

506 **Microscopy**

507 *Leica SP8 confocal microscopy*

508 We conducted confocal or gated STED imaging using a Leica TCS SP8 STED 3 X microscope,
509 controlled by LAS X software. The setup included an HC PL APO 100x/1.4 oil STED WHITE
510 objective, with white laser excitation at 488, 577, and 633 nm and depletion at 775 nm using
511 a pulsed laser. Images were captured in 2D STED mode with a vortex phase mask. The Leica
512 PMT and HyD hybrid detector were used, with a time gate range of 0.5 to 9 ns, and depletion
513 laser power was set at 50%. Images were primarily acquired using confocal microscopy;
514 instances where STED mode was used are explicitly noted in the figure legends.

515 *Airyscan confocal microscopy*

516 A Carl Zeiss LSM880 Fast AiryScan microscope equipped with 405 nm, Argon Multiline, 561
517 nm, and 633 nm lasers as well as AiryScan and PMT detectors was utilized for fixed confocal
518 imaging. Samples were imaged using an Alpha Plan-APO 100x/1.46 Oil DIC VIS objective, and
519 the microscope was operated by ZEN 2.3 software. Images acquired using Airyscan mode are
520 indicated in the figure legends.

521 *Spinning disc microscopy*

522 Spinning disc microscopy was utilized for all live cell imaging experiments. This was performed
523 on a Nikon Eclipse Ti-E inverted research microscope with a Nikon Perfect Focus System, a
524 Nikon Plan Apo VC 100x N.A. 1.40 oil objective, and a spinning disk confocal scanner unit (CSU-
525 X1-A1, Yokogawa). The system featured a Photometrics PRIME BSI back-illuminated sCMOS
526 camera, an ASI motorized stage with piezo plate MS-2000-XYZ, and MetaMorph 7.10
527 software. It was equipped with three lasers: a 488 nm, 150 mW Vortran Stradus 488; a 561
528 nm, 100 mW Coherent OBIS 561-100LS; and a 639 nm, 150 mW Vortran Stradus 639. For
529 imaging, we used the ET-GFP filter set (49002, Chroma) for GFP-tagged proteins, the ET-
530 mCherry filter set (49008, Chroma) for mCherry-tagged proteins, and the ET-Cy5 filter set
531 (49006, Chroma) for HaloTag JF646-tagged proteins. To maintain the cells at 37°C we used a
532 stage incubator (STXG-PLAMX-SETZ21L, Tokai Hit). For localized illumination experiments the
533 iLas FRAP system controlled with iLas software (Gataca Systems) was used.

534 *Optogenetic vimentin pulling*

535 For whole cell illumination fixed experiments cells were either protected from light and fixed
536 in a dark room with only red and green light (DARK) OR placed on a blue LED array and
537 illuminated for 45 minutes (800 µW/cm^2) (LIT). Live cell imaging experiments were performed
538 on a spinning disc microscope, using a 488 nm laser to activate iLID-SspB. For whole cell
539 activation either one 500 ms exposure (0.25 mW, 300 µW/cm^2) every 4 s or one 1 s exposure

540 (0.25 mW, 300 µW/cm^2) every 30 s was used. For localized activation a FRAP unit was used to
541 apply one localized scan with a duration of 113 ms (3 µW, 700 µW/cm^2) every 4 s.

542 **Cell stiffness measurements**

543 U2OS cells were seeded in 35 mm glass-bottom dishes (World Precision Instruments) and
544 allowed to adhere overnight. Cells were subsequently transfected as described above, and
545 stiffness measurements were performed the following day. The Young's modulus of cells
546 before and after vimentin pulling was measured using a Chiaro Nanoindenter (Optics11 Life).
547 We indented cells with a spherical tip with 3.5 µm radius, attached to a flexible cantilever
548 with a stiffness of 0.027 N/m. Indentations were made with a loading rate of 2 µm/s to a
549 depth of 1.5 µm. For vimentin-pulled cells, we waited 30 minutes after adding rapalog before
550 performing indentation measurements. The Chiaro Nanoindenter was mounted on a
551 THUNDER epifluorescence microscope (Leica), allowing us to identify transfected cells. Cells
552 selected for indentation were successfully co-transfected with Vim-mCh-FKBP and FRB-BFP-
553 GCN4-ppKin14Young's modulus was calculated from measured force-distance curves using
554 the Hertzian contact model by the Optics11 Life Dataviewer software (version 2). Each cell
555 was indented at three separate locations in the perinuclear region. Measurements without a
556 distinct contact point or with an otherwise unreliable model fit (<0.9 R^2) were regarded as
557 outliers and excluded from the analysis.

558 **Quantification and statistical analysis**

559 FIJI software was utilized to adjust contrast levels and perform background corrections for
560 image and video preparation. Fluorescence intensity quantification was also carried out in
561 FIJI, with subsequent data processing and normalization completed in Excel. Statistical
562 analysis and graph generation were performed using GraphPad Prism 10.1.1 (323). The Mann-
563 Whitney test was applied for comparisons between two conditions, whereas the Kruskal-
564 Wallis test, followed by Dunn's multiple comparisons test, was used for comparing more than
565 two conditions.

566 *Analysis of fluorescence intensities of transfected constructs*

567 Vim-mCh-SspB, Vim-mCh-FKBP, FRB-BFP-GCN4-ppKin14, iLID-GFP-GCN4-ppKin14, KIF5A-
568 mVenus-iLID, HA-KIF5A-FRB (stained with anti-HA antibody) fluorescence intensities were
569 quantified by defining regions of interest (ROI) around individual cells, including transfected
570 and non-transfected neighboring cells, and a background region for normalization. The mean
571 gray value was measured for each ROI using the following equation:

572 $$Normalized\ intensity = \frac{(transfected\ cell\ intensity - background)}{(untransfected\ neighbour\ intensity - background)}$$

573 *Quantification of the fraction cell area occupied by vimentin*

574 To quantify the area occupied by vimentin, we thresholded the total vimentin intensity (as
575 obtained by immunofluorescence staining) using the Li threshold algorithm in Fiji and then

576 quantified the total vimentin area using the "Detect Particles" function. This value was then
577 divided by total cell area to calculate cell area occupied by vimentin.

578 *Quantification of vimentin recovery at the cell periphery*

579 Vimentin at cell periphery was analyzed by drawing a ROI near the cell edge, at the cell edge
580 furthest from the MTOC / vimentin cluster, between 10-15 µm in width where the width was
581 perpendicular to the cell edge. ROI was adjusted during cell movement, mean grey value was
582 measured over time inside ROI. Background was subtracted from the measurement and then
583 normalized to the first time point.

584 *Quantification of focal adhesion number*

585 We utilized the ComDet plugin for Fiji (https://github.com/ekatrukha/ComDet) to detect the
586 total number of focal adhesions based on paxillin staining. Phalloidin staining was employed
587 to help define the total cell area. The total number of focal adhesions was then normalized
588 by dividing it by the cell area.

589 *Analysis of microtubule intensity and radiality*

590 To quantify the intensity of tyrosinated tubulin, we used ROIs around transfected and non-
591 transfected cells and background areas. The mean grey value for each ROI was measured and
592 used in the following formula:

593 $$Normalized\ intensity = \frac{(transfected\ cell\ intensity - background)}{(untransfected\ neighbour\ intensity - background)}$$

594 To quantify the total intensity of the radial and non-radial microtubules we used the radiality
595 map plugin (https://github.com/UU-cellbiology/radialitymap). After defining radial and non-
596 radial microtubules, we calculated the ratio by dividing the mean intensity of non-radial
597 microtubules by the mean intensity of radial microtubules over the same cell area.

598 For the quantification of acetylated tubulin, the mean gray values observed after background
599 subtraction were normalized to the average acetylated tubulin intensity in non-transfected
600 cells.

601 *Analysis of vimentin and keratin co-localization*

602 Manders colocalization coefficients for keratin-8 and vimentin networks were calculated
603 using the JACoP plugin in Fiji (Bolte and Cordelières, 2006). Before measuring colocalization,
604 we manually thresholded the images to accurately define the keratin-8 and vimentin
605 networks. Coefficients were calculated from ROIs with dimensions of 50.2 × 50.2 µm for COS-
606 7 cells, 45.11 × 45.11 µm for U2OS cells, and 35.03 × 35.03 µm for HeLa cells, corresponding
607 to their average cell size. Kruskal–Wallis test with Dunn's multiple comparisons test was used
608 to compare the colocalization coefficients of keratin-8 to vimentin for the different
609 conditions.

610 *Analysis of perinuclear to peripheral ER/vimentin intensity*

611 A circle with a diameter of 27.9 µm was drawn around the nucleus/perinuclear cloud to
612 quantify fluorescence intensity at the perinuclear area. A mask of the cell was created with
613 the perinuclear area removed to quantify the fluorescence intensity at the cell periphery. A
614 region outside the cell was drawn to quantify background fluorescence. The ratio of intensity
615 at the perinuclear region to intensity at the cell periphery was then calculated as follows:

616 $$Ratio\ perinuclear\ region\ to\ cell\ periphery = \frac{perinuclear\ intensity - background}{periphery\ intensity - background}$$

617 *Analysis of ER and tagged vimentin intensity during localized vimentin pulling*

618 Localized opto-vimentin pulling experiment in cells co-transfected with Halo-KDEL was
619 analyzed by quantifying mean grey value of Vim-mCh-SspB and Halo-KDEL inside blue light
620 (488 nm) illuminated region over time. Background was subtracted and values were
621 normalized to the first time point.

622 *Analysis of lysosome and mitochondria distribution*

623 Distributions of mitochondria and lysosomes was analyzed using LAMTOR4 and Cytochrome
624 C staining, respectively. The ComDet plugin was used to detect particles, with the cell center
625 defined at the MTOC. A radius macro was used to calculate the distance of each particle from
626 the cell (https://gist.github.com/ekatrukha/105553627f1bee01367faae153bfe5c0).

627 From these distance measurements, we determined the fraction of particles located in the
628 cell periphery. The peripheral region was defined as an area beyond a circle with 13.81 µm
629 radius from the MTOC, based on the average size of the perinuclear cloud for U2OS cells.
630 Particles outside this circle were classified as being in the peripheral area of the cell.

631

Author contributions

M.P. and J.C.M.M. designed and performed experiments, analyzed data and wrote the paper, J.P.C. and G.H.K. performed and analyzed cell stiffness measurements and wrote the paper, A.A. coordinated the project and wrote the paper.

Acknowledgements

We thank L. Kapitein and G. G. Farías (Utrecht University) for providing materials, I. Berlin (Leiden University Medical Center) for sharing RNF26 knockout U2OS cells, and Eugene Katrukha (Utrecht University) for technical support and guidance on image analysis. This work was supported by the Netherlands Organization for Scientific Research (NWO) project ECHO 711018004, EMBO long-term fellowship ALTF 261-2019, OCENW.M20.054, Gravitation programme IMAGINE! (project number 24.005.009), the European Research Council Synergy grant PushingCell (project number 101071793) to A.A. and a grant of NWO Talent Programme (project number VI.C.182.004) to G.H.K.

Competing interests

The authors declare no competing interests.

Figure Legends

Figure 1. Repositioning of the vimentin network by rapalog-induced recruitment of kinesin motors.

(A) A scheme of rapalog-induced heterodimerization constructs. A truncated motor domain of *Physcomitrella patens* kinesin-14b (ppKin14, amino acids 861–1321) is fused to the FRB domain, along with a GCN4 leucine zipper for tetramerization and a BFP tag for detection. A fragment of human KIF5A (amino acids 1–560) is fused to an HA-tagged dimeric motor domain and the FRB domain. The FKBP domain and mCherry were fused to the C-terminus of vimentin. Flexible GS linkers separate protein domains.

(B, C) Schemes illustrating vimentin repositioning triggered by rapalog-induced recruitment of kinesins at the level of a single microtubule **(B)** and in whole cells **(C)**. Without rapalog, Vim-mCh-FKBP does not interact with either FRB-BFP-GCN4-ppKin14 or HA-KIF5A-FRB. Upon rapalog addition, FRB and FKBP heterodimerize, triggering motor attachment to vimentin filaments and their movement along microtubules. Minus-end-directed kinesins trigger vimentin clustering around the MTOC, whereas plus-end-directed kinesins cause the formation of small peripheral clusters and a large perinuclear one.

(D, E) Representative fluorescence images of COS-7 cells co-transfected with Vim-mCh-FKBP and FRB fusions of the indicated motors, with or without 1 hour rapalog treatment. The top panels show untreated cells, whereas the bottom panels display rapalog-treated cells. Transfected cells are outlined with dashed lines, and non-transfected cells serve as controls. Anti-vimentin and anti-HA antibodies detect total vimentin and HA-KIF5A-FRB, respectively.

(F) Quantifications of the fraction of the cell area occupied by vimentin in untransfected and transfected cells with either minus- or plus-end motor constructs, with and without rapalog treatment.

(G-I) Mean fluorescence intensities of Vim-mCh-FKBP intensity **(G)**, FRB-BFP-GCN4-ppKin14 **(H)** and HA-KIF5A-FRB, detected with anti-HA antibody **(I)** per cell, normalized to untransfected cells.

In **(F-I)**, n = 19–34 cells per condition across 3 independent experiments. Plots indicate mean±SD with individual cell measurements shown as dots. ns, not significant; $*$, $p < 0.05$; $****$, $p < 0.0001$.

(J-L) Live cell imaging reveals the morphology of the vimentin network immediately before and at 10, 20, and 60 min after rapalog addition. Cells co-transfected with ppKin14 **(J)** or KIF5A constructs **(L)** show vimentin reorganization over time.

(K, M) Total vimentin distribution in cells shown in **(J)** and **(L)**, fixed and stained with antibodies against vimentin 60 minutes after rapalog treatment.

683 **Figure 2. Reversible vimentin repositioning by optogenetic recruitment of kinesin motors to**
684 **vimentin.**

685 **(A**) Schematic overview of optogenetic vimentin constructs. The constructs are similar to
686 those shown in Figure 1A, except that FRB is substituted for iLID and FKBP for SSB_{micro}. GFP
687 and mVenus are used as fluorescent markers in ppKin14 and KIF5A constructs, respectively.

688 **(B, C)** Schematics illustrating the action of the optogenetic vimentin constructs. **(B)** Upon blue
689 light activation the iLID module changes conformation, uncaging a SsrA peptide, which binds
690 to SspB. By tagging vimentin with SspB and ppKin14 and KIF5A with iLID, vimentin can be
691 inducibly pulled towards microtubule minus or plus ends, respectively. **(C)** Transfection of cells
692 with Vim-mCh-SspB combined with one of the two kinesin constructs and blue light activation
693 results in vimentin pulling to microtubule minus or plus-ends, causing vimentin clustering
694 either at the MTOC (ppKin14) or both cell periphery and MTOC (KIF5A).

695 **(D)** U2OS cells expressing Vim-mCh-SspB construct. The overexpressed vimentin network is
696 visualized by mCherry fluorescence, while total vimentin intensity is detected via anti-
697 vimentin immunostaining. Images were captured using scanning confocal microscopy.

698 **(E-I)** U2OS cells co-transfected with Vim-mCh-SspB and iLID-GFP-GCN4-ppKin14 were either
699 fixed in a dark room (DARK) or exposed to 45 minutes of blue light (LIT) prior to fixation and
700 staining for vimentin (Total vimentin). **(E)** Representative images, with transfected cells
701 outlined with a dashed line. **(F)** Quantification of the fraction of the cell area occupied by
702 vimentin. **(G)** Mean iLID-GFP-GCN4-ppKin14 fluorescence intensity per cell, normalized to
703 untransfected cells. **(H)** Mean cell Vim-mCh-SspB fluorescence intensity. **(I)** Mean total cell
704 area. **(F-I)** n=23-29 cells per treatment analyzed over 3 experiments; bars show mean ± SD. ns,
705 not significant; ****, $p < 0.0001$.

706 **(J-L)** U2OS cells co-transfected with Vim-mCh-SspB and iLID-GFP-GCN4-ppKin14 were locally
707 illuminated with 488 nm light pulses for 40 minutes before fixing and staining for vimentin. **(J)**
708 Scheme of the experiment. **(K)** Stills with the region illuminated with blue light indicated with
709 a blue dashed box. **(L)** Vimentin staining in the cell shown in **(K)** fixed after local illumination.

710 **(M-N)** U2OS cells co-transfected with Vim-mCh-SspB and iLID-GFP-GCN4-ppKin14 were
711 exposed to whole cell 488 nm light pulses for 30 min to cluster vimentin, and then 488 nm
712 pulses were stopped to allow cells to recover over 4 hours. **(M)** Representative cell directly
713 before light pulses (-30 min), after 30 minutes of 488 nm light pulsing (0 min) and after 4 hours
714 of recovery without blue light activation (4 h). **(N)** Quantification of Vim-mCh-SspB mean
715 intensity at a ROI at the cell periphery over time; plot shows a line for every individual cell, n
716 = 9 cells analyzed over 3 independent experiments.

717

718 **Figure 3. Effects of vimentin repositioning on the microtubule cytoskeleton.**

(A, B) COS-7 cells were co-transfected with Vim-mCh-FKBP and either FRB-BFP-GCN4-ppKin14 **(A)** or HA-KIF5A-FRB **(B)**, with non-transfected cells as controls. Transfected cells are outlined with a dashed line. After one hour of treatment with or without rapalog, cells were fixed for analysis. Representative fluorescent images display the microtubule network, labeled with antibodies against tyrosinated α-tubulin (Tyr-tubulin). Microtubules are further color-coded to indicate radial (cyan) and non-radial (yellow) orientations.

(C) Quantification of tyrosinated α-tubulin intensity in cells expressing Vim-mCh-FKBP along with either FRB-BFP-GCN4-ppKin14 or HA-KIF5A-FRB, normalized to non-transfected cells, with or without rapalog treatment. n = 21-23 cells analyzed across two independent experiments.

(D) Quantification of the ratio of non-radial to radial tyrosinated microtubules in non-transfected cells and cells expressing Vim-mCh-FKBP with either FRB-BFP-GCN4-ppKin14 or HA-KIF5A-FRB, with or without rapalog treatment. n = 20-22 cells were analyzed across two independent experiments.

(E, F) Representative images of U2OS cells stained for acetylated microtubules (Ac-tubulin), showing either untransfected cells or cells co-expressing Vim-mCh-FKBP with either FRB-BFP-GCN4-ppKin14 **(E)** or HA-KIF5A-FRB **(F)**. Transfected cells are outlined with a dashed line. After one hour of treatment with or without rapalog, cells were fixed for analysis.

(G) Quantification of normalized acetylated microtubule intensity in untransfected U2OS cells and cells co-expressing Vim-mCh-FKBP with either FRB-BFP-GCN4-ppKin14 or HA-KIF5A-FRB, in the presence and absence of rapalog. n = 37-49 cells were analyzed across three independent experiments. Plots indicate mean ± SD with individual cell measurements shown as dots. ns, not significant; $*$, $p < 0.05$; $**$, $p < 0.01$; $***$, $p < 0.001$; $****$, $p < 0.0001$.

Figure 4. Effects of vimentin repositioning on the actin cytoskeleton, cell spreading, and focal adhesions.

COS-7 **(A-C)** or U2OS **(D-F)** cells were co-transfected with Vim-mCh-FKBP and FRB-BFP-GCN4-ppKin14, while non-transfected cells served as controls. Transfected cells are outlined with a dashed line.

(A, D) After one hour of treatment with or without rapalog, the cells were fixed and stained for total vimentin, paxillin, and actin using phalloidin.

(B, E) Quantification of the total cell area based on the phalloidin staining in transfected (T) and untransfected (U) cells, with and without rapalog treatment. Dashed boxes show regions enlarged in the Zoom panels.

(C, F) Quantification of the total focal adhesion number based on paxillin staining, normalized to cell area as determined by phalloidin staining in both transfected and untransfected cells,

755 with or without rapalog treatment. Measurements were collected from n = 28-31 cells in **(B)**
756 and **(C)**, and from n = 27-29 cells in **(E)** and **(F)**, across three independent experiments. The
757 plots display the mean ± SD, with individual cell measurements represented as dots. ns, not
758 significant.

759

760 **Figure 5. Effects of vimentin clustering on the keratin-8 network across cell lines.**

761 **(A, C, E)** Indicated cell lines were co-transfected with Vim-mCh-FKBP and FRB-BFP-GCN4-
762 ppKin14 constructs (outlined), while non-transfected cells served as controls. After one hour
763 of treatment with or without rapalog, the cells were fixed for analysis. Total vimentin and
764 keratin-8 network intensities were measured after staining with anti-vimentin and anti-
765 keratin-8 antibodies, respectively. White dashed box indicates the region of the cell enlarged
766 in zoom images. Images were obtained with Airyscan mode.

767 **(B, D, F)** Colocalization analysis in COS-7 **(B)**, U2OS **(D)** and HeLa **(F)** cells. The graphs represent
768 Manders' coefficients of thresholded images, measured from 50.2 × 50.2 µm ROIs per COS-7
769 cell **(B),** 45.11 × 45.11 µm ROIs per U2OS cell **(D)** and 35.03 × 35.03 µm ROIs per HeLa cell **(F)**.
770 Data are shown as mean ± SD, with individual cell measurements represented by dots. In panel
771 **(B)**, data were collected from n = 25–29 cells; in panel **(D)**, n = 27–29 cells; and in panel **(F)**, n
772 = 27–34 cells, across three independent experiments. ns, not significant; ∗, $p < 0.05$;∗∗, $p <$
773 0.01; ∗∗∗∗, $p < 0.0001$.

774

775 **Figure 6. Effects of vimentin repositioning on cell stiffness.**

776 **(A, B)** Schematic depiction of a control and a rapalog-treated U2OS cell co-transfected with
777 Vim-mCh-FKBP and FRB-BFP-GCN4-ppKin14, before and during indentation in the perinuclear
778 region using a spherical tip of 3.5 µm radius. Each cell was indented at three separate locations
779 in the perinuclear region.

780 **(C)** The graph presents the Young's modulus of cells co-transfected with Vim-mCh-FKBP and
781 FRB-BFP-GCN4-ppKin14 constructs, with and without rapalog treatment. Data were collected
782 from n = 19-22 cells across two independent experiments. A total of 56 measurements were
783 obtained from 19 cells without rapalog, and 63 measurements from 22 cells treated with
784 rapalog. The plots display the mean ± SD, with each dot representing an individual cell
785 measurement. ****, $p < 0.0001$.

786

787 **Figure 7. Effects of vimentin repositioning on ER morphology.**

788 **(A)** Representative image of a COS-7 cell stained for endogenous calnexin (ER) and vimentin,
789 and **(B)** intensity profile along the indicated line. Images were collected using STED.

(C-E) U2OS cell co-transfected with Vim-mCh-SspB, iLID-GFP-GCN4-ppKin14 and Halo-KDEL was first imaged for 5 minutes without 488 nm pulsing (-5 min, 0 min), then imaged for 25 minutes with whole cell 488 nm pulsing to induce optogenetic vimentin clustering (5 min, 10 min, 25 min). **(C)** Spinning disc confocal images from experiment, with black dashed boxes indicating the region of the cell enlarged in the zoom panels. **(D)** Plot showing ratio of perinuclear fluorescence intensity to intensity at the cell periphery. **(E)** Plot showing loss of total fluorescence signal over time.

(F) Images of COS-7 cells expressing Vim-mCh-FKBP and FRB-BFP-GCN4-ppKin14. Transfected cells are outlined with dashed lines. After one hour of treatment with or without rapalog, cells were fixed and stained for vimentin and calnexin. The images show the distribution of the ER network, visualized by calnexin staining, in both transfected (T) and untransfected (U) cells, in the presence and absence of rapalog. Dashed boxes show the regions that have been enlarged and shown as masks in the zoom images.

Figure 8. Localized optogenetic vimentin repositioning displaces dense ER matrices independent of RNF26.

(A-C) U2OS wild type (WT) **(A)** and RNF26 knockout (KO) **(B)** cells co-transfected with Vim-mCh-SspB, iLID-GFP-GCN4-ppKin14 and Halo-KDEL were pulsed with 488 nm light inside a region of interest at the cell periphery (blue dashed box) for 20 minutes in order to locally displace vimentin. **(A-B)** Example images shown before blue light pulsing (0 min) and 5, 10 and 20 min after localized blue light application. Black dashed box indicates the region of the cell enlarged in zoom images. **(C)** Mean fluorescence intensity of Vim-mCh-SspB and Halo-KDEL (ER) inside the ROI pulsed with blue light was quantified over time and normalized to the first time point after subtracting background. Graph shows mean ± SD, n = 8-9 cells analyzed per group over 3 independent experiments.

Figure 9. Effects of vimentin clustering on the distribution of mitochondria and lysosomes.

(A, D) U2OS cell, co-transfected with Vim-mCh-SspB, iLID-GFP-GCN4-ppKin14 and Halo-MitoTag to label mitochondria **(A)** or LAMP1-Halo to label lysosomes **(D)**, locally illuminated with 488 nm pulses inside a region of interest (blue dashed box) for 10 min **(A)** or with global illumination for 20 min **(D)**. The cell is shown before application of blue light (0 min) and at the indicated time points after blue light pulsing.

(B, E) Imaging of U2OS cells transfected with Vim-mCh-FKBP and FRB-BFP-GCN4-ppKin14 constructs. After one hour of treatment with or without rapalog, cells were subjected to immunostaining for total vimentin and Cytochrome C to label mitochondria **(B)** or LAMTOR4 to label lysosomes **(E)**. Transfected cells are indicated by a dotted outline. Images were acquired with Airyscan mode.

827 **(C, F)** The distribution of mitochondria **(C)** or lysosomes **(F)** relative to the MTOC. Organelles
828 were detected using the ComDet plugin, and their distance from the MTOC was calculated
829 using a radius plugin. The graph shows the percentage of mitochondria or lysosomes located
830 in the peripheral region, which was defined as an area beyond a 13.81 µm radius from the
831 MTOC, with each dot representing data from an individual cell. Measurements were collected
832 from n = 20-29 cells in **(C)**, and from n = 20-22 cells in **(F)**, across three independent
833 experiments. The plots display the mean ± SD, with individual cell measurements represented
834 as dots. ns, not significant; $**$, $p < 0.01$.

835 **Legends to Supplementary Figures.**

836 **Figure S1. Motor recruitment to the filaments with the rapalog system and repositioning of**
837 **the vimentin network in U2OS cells.**

838 **(A)** Fluorescence images of COS-7 cells expressing Vim-mCh-FKBP construct. The
839 overexpressed vimentin network is visualized by mCherry fluorescence, while total vimentin
840 intensity is detected via anti-vimentin immunostaining. Dashed box indicates the region of the
841 cell enlarged in zoom image. Images were captured using Airyscan microscopy.

842 **(B-C)** Fluorescence images of COS-7 cells co-transfected with Vim-mCh-FKBP and either FRB-
843 GFP-GCN4-ppKin14 **(B)** or HA-KIF5A-FRB **(C)**, with or without 5-minute rapalog treatment. The
844 top panels show untreated cells, while the bottom panels display rapalog-treated cells. FRB-
845 GFP-GCN4-ppKin14 and HA-KIF5A-FRB are detected using anti-GFP and anti-HA antibodies.
846 Images were captured using Airyscan microscopy.

847 **(D-E)** Representative fluorescence images of U2OS cells co-transfected with Vim-mCh-FKBP
848 and FRB fusions of the indicated motors, with or without 1 hour rapalog treatment. The top
849 panels show untreated cells, while the bottom panels display rapalog-treated cells.
850 Transfected cells are outlined with dashed lines, and non-transfected cells serve as controls.
851 Anti-vimentin and anti-HA antibodies detect total vimentin and HA-KIF5A-FRB, respectively.

852 **Figure S2. Optogenetic minus-end-directed motor recruitment and vimentin pulling by plus-**
853 **end-directed kinesin.**

854 **(A)** U2OS cells co-transfected with Vim-mCh-SspB and iLID-GFP-GCN4-ppKin14 were either
855 fixed in a dark room (DARK) or exposed to 5 minutes of blue light (LIT) prior to fixation and
856 staining for anti-GFP. Zoomed-in views, highlighted by the dashed box, show the region of the
857 cell enlarged in the zoom panel. Images were captured using Airyscan confocal microscopy.

858 **(B)** U2OS cells co-transfected with Vim-mCh-SspB and iLID-GFP-GCN4-ppKin14 and imaged
859 live using spinning disc confocal microscopy. Cells were illuminated for 30 minutes in 4 second
860 pulses over the entire cell, then allowed to recover their vimentin distribution in the absence
861 of blue light stimulation for 4 hours. Graph shows quantification of construct expression levels
862 based on fluorescence at the first frame with background subtracted. Cells were categorized
863 either as having no vimentin clustering (red square), vimentin pulling with recovery of
864 vimentin spreading after 4 hours (blue circle) or vimentin pulling without complete recovery
865 of vimentin spreading after 4 hours (green triangle).

866 **(C-D)** Schematic of overview of constructs for optogenetic plus end directed vimentin pulling.

867 **(E)** U2OS cells co-transfected with Vim-mCh-SspB and KIF5A-mVenus-iLID show vimentin re-
868 localization to clusters in the cell periphery and at the cell center upon blue light activation.
869 Live cell imaging stills shown before blue light activation (0 min) and 10 and 30 minutes after
870 488 nm pulsing.

871 **Figure S3. KIF5A overexpression affects the stable microtubule network.**

872 **(A)** Representative images of U2OS cells, either untransfected or transfected with HA-KIF5A-
873 FRB, stained for acetylated microtubules (Ac-tubulin). Transfected cell is outlined with a
874 dashed line.

875 **(B)** Quantification of normalized acetylated microtubule intensity in untransfected U2OS cells
876 and HA-KIF5A-FRB-expressing cells. A total of 31–32 cells were analyzed across three
877 independent experiments. Data are presented as mean ± SD, with individual cell
878 measurements shown as dots. **** $p < 0.0001$.

879 **Figure S4. Endogenous vimentin and keratin-8 filament networks in COS-7, U2OS, and HeLa**
880 **cells**

881 **(A)** Expression levels of vimentin and keratin-8 in COS-7, U2OS, and HeLa cells analyzed by
882 Western blotting.

883 **(B-G)** Airyscan high-resolution images of vimentin and keratin-8 networks in COS-7 **(B)**, U2OS
884 **(D)**, and HeLa cells **(F)**, detected by staining with anti-vimentin and anti-keratin-8 antibodies,
885 respectively**.** Zoomed-in views (5x5 µm), highlighted by the dashed box, showing the region
886 of the cell enlarged in the zoom panel and intensity profiles for vimentin and keratin-8 along
887 the indicated lines in COS-7 **(C)**, U2OS **(E),** and HeLa **(G)** cells.

888 **Figure S5. A force-distance curve for cell stiffness measurements.**

889 An example force curve used to determine the Young's modulus of the cells. The raw data is
890 shown in blue and the Hertz model fit is the red line. Fitting was restricted to the first 1.5 µm
891 of indentation, as shown in the figure.

892 **Source data Figure S4.**

893 Complete uncropped blots shown in Figure S4A.

894

895 **Legends to Videos.**

896 **Video 1. Rapalog-induced vimentin repositioning by minus-end-directed kinesin.**

897 COS-7 cell co-expressing Vim-mCh-FKBP and FRB-BFP-GCN4-ppKin14. Imaging was conducted
898 for a total of 70 minutes, rapalog is added at the 10-minute mark. Time is shown in hh:mm:ss.

899 **Video 2. Rapalog-induced vimentin repositioning by plus-end-directed kinesin.**

900 COS-7 cell co-expressing Vim-mCh-FKBP and HA-KIF5A-FRB. Total imaging time: 70 minutes,
901 rapalog is added at the 10-minute mark. Time is shown in hh:mm:ss.

902 **Video 3. Rapalog-induced vimentin repositioning by plus-end-directed kinesin.**

903 COS-7 cell co-expressing Vim-mCh-FKBP and HA-KIF5A-FRB. Movie starts from the moment
904 rapalog is added. Time is shown in hh:mm:ss.

905 **Video 4. Light-induced vimentin repositioning and recovery.**

906 U2OS cell co-expressing Vim-mCh-SspB and iLID-GFP-GCN4-ppKin14 was exposed to 1 s of
907 whole cell blue light illumination every 30 s for a total of 30 minutes; a blue dot is shown in
908 the top right corner during blue light illumination. The cell was subsequently imaged for
909 another 4 hours without blue light activation to allow vimentin distribution to recover. Time
910 is shown in hh:mm.

911 **Video 5. Effect of light-induced vimentin repositioning on ER.**

912 U2OS cell co-transfected with Vim-mCh-SspB, iLD-GFP-GCN4-ppKin14 and Halo-KDEL (ER
913 marker) was first imaged for 5 min without blue light, then imaged for another 25 min with
914 500 ms of whole cell blue light illumination every 4 s; the period of blue light pulsing is
915 indicated by a blue dot in the top right corner. Time is shown in mm:ss.

916 **Video 6. Effect of local light-induced vimentin repositioning on ER in a control cell.**

917 Wild type U2OS cell co-transfected with Vim-mCh-SspB, iLD-GFP-GCN4-ppKin14 and Halo-
918 KDEL (ER marker) was illuminated inside a region of interest (indicated by blue box) with
919 one 113 ms pulse of blue light every 4 s; period of blue light pulsing is indicated by a blue
920 dot in the top right corner. Time is shown in mm:ss.

921 **Video 7. Effect of local light-induced vimentin repositioning on ER in an RNF26 knockout**
922 **cell.**

923 RNF26 KO U2OS cell co-transfected with Vim-mCh-SspB, iLD-GFP-GCN4-ppKin14 and Halo-
924 KDEL (ER marker) was illuminated inside a region of interest (indicated by blue box) with
925 one 113 ms pulse of blue light every 4 s; period of blue light pulsing is indicated by a blue
926 dot in the top right corner. Time is shown in mm:ss.

927 **Video 8. Effect of local light-induced vimentin repositioning on mitochondria.**

928 U2OS cell co-transfected with Vim-mCh-SspB (magenta), iLD-GFP-GCN4-ppKin14 and Halo-
929 MitoTag (cyan, mitochondria marker) was illuminated inside a region of interest (indicated
930 by blue box) with one 113 ms pulse of blue light every 4 s; period of blue light pulsing is
931 indicated by a blue dot in the top right corner. Time is shown in mm:ss.

932 **Video 9. Effect of light-induced vimentin repositioning on lysosomes.**

933 U2OS cell co-transfected with Vim-mCh-SspB (cyan), iLD-GFP-GCN4-ppKin14 and LAMP1-
934 Halo (yellow, lysosome marker) was exposed to 500 ms of blue light illumination every 4 s;
935 period of blue light pulsing is indicated by a blue dot in the top right corner. Time is shown
936 in mm:ss.

937

References

Andreu-Carbó, M., C. Egoldt, M.-C. Velluz, C. Aumeier, M. Andreu-Carbó, C. Egoldt, M.-C. Velluz, and C. Aumeier. 2024. Microtubule damage shapes the acetylation gradient. *Nat Commun*. 15:2029.

Aufderhorst-Roberts, A., and G.H. Koenderink. 2019. Stiffening and inelastic fluidization in vimentin intermediate filament networks. *Soft Matter*. 15:7127-7136.

Bargagna-Mohan, P., A. Hamza, Y. Kim, Y. Ho, N. Mor-Vaknin, N. Wendschlag, J. Liu, R.M. Evans, D.M. Markovitz, C.-G. Zhan, K.B. Kim, and R. Mohan. 2007. The tumor inhibitor and antiangiogenic agent withaferin A targets the intermediate filament protein vimentin. *Chem Biol*. 14:623-634.

Bhattacharya, R., A.M. Gonzalez, P.J. DeBiase, H.E. Trejo, R.D. Goldman, F.W. Flitney, and J.C.R. Jones. 2009. Recruitment of vimentin to the cell surface by β3 integrin and plectin mediates adhesion strength. *J Cell Sci*. 122:1390-1400.

Bolte, S., and F.P. Cordelières. 2006. A guided tour into subcellular colocalization analysis in light microscopy. *J Microsc*. 224:213-232.

Bomont, P. 2016. Degradation of the Intermediate Filament Family by Gigaxonin. *Methods Enzymol*. 569:215-231.

Cai, D., D.P. McEwen, J.R. Martens, E. Meyhofer, and K.J. Verhey. 2009. Single molecule imaging reveals differences in microtubule track selection between Kinesin motors. *PLoS Biol*. 7:e1000216.

Chen, F., J. Wu, M.K. Iwanski, D. Jurriens, A. Sandron, M. Pasolli, G. Puma, J.Z. Kromhout, C. Yang, W. Nijenhuis, L.C. Kapitein, F. Berger, and A. Akhmanova. 2022. Self-assembly of pericentriolar material in interphase cells lacking centrioles. *eLife*. 11:e77892.

Cheng, F., and J.E. Eriksson. 2017. Intermediate Filaments and the Regulation of Cell Motility during Regeneration and Wound Healing. *Cold Spring Harb Perspect Biol*. 9:a022046.

Clackson, T., W. Yang, L.W. Rozamus, M. Hatada, J.F. Amara, C.T. Rollins, L.F. Stevenson, S.R. Magari, S.A. Wood, N.L. Courage, X. Lu, F. Cerasoli, Jr., M. Gilman, and D.A. Holt. 1998. Redesigning an FKBP-ligand interface to generate chemical dimerizers with novel specificity. *Proc Natl Acad Sci U S A*. 95:10437-10442.

Colucci-Guyon, E., M.M. Portier, I. Dunia, D. Paulin, S. Pournin, and C. Babinet. 1994. Mice lacking vimentin develop and reproduce without an obvious phenotype. *Cell*. 79:679-694.

Cremer, T., L.M. Voortman, E. Bos, M.L. Jongsma, L.R. Ter Haar, J.J. Akkermans, C.M. Talavera Ormeno, R.H. Wijdeven, J. de Vries, R.Q. Kim, G.M. Janssen, P.A. van Veelen, R.I. Koning, J. Neefjes, and I. Berlin. 2023. RNF26 binds perinuclear vimentin filaments to integrate ER and endolysosomal responses to proteotoxic stress. *EMBO J*. 42:e111252.

De Pascalis, C., C. Pérez-González, S. Seetharaman, B. Boëda, B. Vianay, M. Burute, C. Leduc, N. Borghi, X. Trepat, and S. Etienne-Manneville. 2018. Intermediate filaments control collective migration by restricting traction forces and sustaining cell-cell contacts. *J Cell Biol*. 217:3031-3044.

Dunn, S., E.E. Morrison, T.B. Liverpool, C. Molina-París, R.A. Cross, M.C. Alonso, and M. Peckham. 2008. Differential trafficking of Kif5c on tyrosinated and detyrosinated microtubules in live cells. *J Cell Sci*. 121:1085-1095.

982 Eckes, B., E. Colucci-Guyon, H. Smola, S. Nodder, C. Babinet, T. Krieg, and P. Martin. 2000.
983 Impaired wound healing in embryonic and adult mice lacking vimentin. *J Cell Sci*.
984 113:2455-2462.
985 Eckes, B., D. Dogic, E. Colucci-Guyon, N. Wang, A. Maniotis, D. Ingber, A. Merckling, F. Langa,
986 M. Aumailley, A. Delouvée, V. Koteliansky, C. Babinet, and T. Krieg. 1998. Impaired
987 mechanical stability, migration and contractile capacity in vimentin deficient
988 fibroblasts. *J Cell Sci*. 111:1897-1907.
989 Eibauer, M., M.S. Weber, R. Kronenberg-Tenga, C.T. Beales, R. Boujemaa-Paterski, Y. Turgay, S.
990 Sivagurunathan, J. Kraxner, S. Koster, R.D. Goldman, and O. Medalia. 2024. Vimentin
991 filaments integrate low-complexity domains in a complex helical structure. *Nat Struct*
992 *Mol Biol*. 31:939-949.
993 Esue, O., A.A. Carson, Y. Tseng, and D. Wirtz. 2006. A direct interaction between actin and
994 vimentin filaments mediated by the tail domain of vimentin. *J Biol Chem*. 281:30393-
995 30399.
996 Etienne-Manneville, S. 2018. Cytoplasmic Intermediate Filaments in Cell Biology. *Annu Rev*
997 *Cell Dev Biol*. 34:1-28.
998 Foisner, R., F.E. Leichtfried, H. Herrmann, J.V. Small, D. Lawson, and G. Wiche. 1988.
999 Cytoskeleton-associated plectin: in situ localization, in vitro reconstitution, and
1000 binding to immobilized intermediate filament proteins. *J Cell Biol*. 106:723-733.
1001 Gan, Z., L. Ding, C.J. Burckhardt, J. Lowery, A. Zaritsky, K. Sitterley, A. Mota, N. Costigliola,
1002 C.G. Starker, D.F. Voytas, J. Tytell, R.D. Goldman, and G. Danuser. 2016. Vimentin
1003 Intermediate Filaments Template Microtubule Networks to Enhance Persistence in
1004 Cell Polarity and Directed Migration. *Cell Syst*. 3:252-263.
1005 Goldman, R.D., S. Khuon, Y.H. Chou, P. Opal, and P.M. Steinert. 1996. The function of
1006 intermediate filaments in cell shape and cytoskeletal integrity. *J Cell Biol*. 134:971-
1007 983.
1008 Grin, B., S. Mahammad, T. Wedig, M. Cleland, L. Tsai, H. Herrmann, and R.D. Goldman. 2012.
1009 Withaferin a alters intermediate filament organization, cell shape and behavior *PloS*
1010 *One*. 7:e39065.
1011 Guntas, G., R.A. Hallett, S.P. Zimmerman, T. Williams, H. Yumerefendi, J.E. Bear, and B.
1012 Kuhlman. 2015. Engineering an improved light-induced dimer (iLID) for controlling
1013 the localization and activity of signaling proteins. *Proc Natl Acad Sci U S A*. 112:112-
1014 117.
1015 Guo, M., Allen J. Ehrlicher, S. Mahammad, H. Fabich, Mikkel H. Jensen, Jeffrey R. Moore,
1016 Jeffrey J. Fredberg, Robert D. Goldman, and David A. Weitz. 2013. The role of
1017 vimentin intermediate filaments in cortical and cytoplasmic mechanics. *Biophys J*.
1018 105:1562-1568.
1019 Gupton, S.L., and C.M. Waterman-Storer. 2006. Spatiotemporal feedback between
1020 actomyosin and focal-adhesion systems optimizes rapid cell migration. *Cell*.
1021 125:1361-1374.
1022 Gyoeva, F.K., and V.I. Gelfand. 1991. Coalignment of vimentin intermediate filaments with
1023 microtubules depends on kinesin. *Nature*. 353:445-448.
1024 Havel, L.S., E.R. Kline, A.M. Salgueiro, and A.I. Marcus. 2014. Vimentin regulates lung cancer
1025 cell adhesion through a VAV2-Rac1 pathway to control focal adhesion kinase activity.
1026 *Oncogene*. 34:1979-1990.
1027 Helfand, B.T., M.G. Mendez, S.N. Murthy, D.K. Shumaker, B. Grin, S. Mahammad, U. Aebi, T.
1028 Wedig, Y.I. Wu, K.M. Hahn, M. Inagaki, H. Herrmann, and R.D. Goldman. 2011.

1029 Vimentin organization modulates the formation of lamellipodia. *Mol Biol Cell*.
1030 22:1274-1289.
1031 Herrmann, H., and U. Aebi. 2004. Intermediate filaments: molecular structure, assembly
1032 mechanism, and integration into functionally distinct intracellular scaffolds. *Annu Rev*
1033 *Biochem*. 73:749-789.
1034 Herrmann, H., H. Bär, L. Kreplak, S.V. Strelkov, and U. Aebi. 2007. Intermediate filaments:
1035 from cell architecture to nanomechanics. *Nat Rev Mol Cell Biol*. 8:562-573.
1036 Herrmann, H., M. Haner, M. Brettel, S.A. Muller, K.N. Goldie, B. Fedtke, A. Lustig, W.W.
1037 Franke, and U. Aebi. 1996. Structure and assembly properties of the intermediate
1038 filament protein vimentin: the role of its head, rod and tail domains. *J Mol Biol*.
1039 264:933-953.
1040 Hookway, C., L. Ding, M.W. Davidson, J.Z. Rappoport, G. Danuser, and V.I. Gelfand. 2015.
1041 Microtubule-dependent transport and dynamics of vimentin intermediate filaments.
1042 *Mol Biol Cell*. 26:1675-1686.
1043 Jiu, Y., J. Lehtimäki, S. Tojkander, F. Cheng, H. Jäälinoja, X. Liu, M. Varjosalo, J.E. Eriksson, and
1044 P. Lappalainen. 2015. Bidirectional Interplay between Vimentin Intermediate
1045 Filaments and Contractile Actin Stress Fibers. *Cell Rep*. 11:1511-1518.
1046 Jones, J.C., and R.D. Goldman. 1985. Intermediate filaments and the initiation of desmosome
1047 assembly. *J Cell Biol*. 101:506-517.
1048 Jonsson, E., M. Yamada, R.D. Vale, and G. Goshima. 2015. Clustering of a kinesin-14 motor
1049 enables processive retrograde microtubule-based transport in plants. *Nat Plants*.
1050 1:15087.
1051 Kapitein, L.C., M.A. Schlager, W.A. van der Zwan, P.S. Wulf, N. Keijzer, and C.C. Hoogenraad.
1052 2010. Probing intracellular motor protein activity using an inducible cargo trafficking
1053 assay. *Biophys J*. 99:2143-2152.
1054 Ketema, M., M. Kreft, P. Secades, H. Janssen, and A. Sonnenberg. 2013. Nesprin-3 connects
1055 plectin and vimentin to the nuclear envelope of Sertoli cells but is not required for
1056 Sertoli cell function in spermatogenesis. *Mol Biol Cell*. 24:2454-2466.
1057 Kilpatrick, B.S., E.R. Eden, A.H. Schapira, C.E. Futter, and S. Patel. 2013. Direct mobilisation of
1058 lysosomal Ca2+ triggers complex Ca2+ signals. *J Cell Sci*. 126:60-66.
1059 Kim, D.-H., and D. Wirtz. 2013. Focal adhesion size uniquely predicts cell migration. *FASEB J*.
1060 27:1351-1361.
1061 Kim, D.I., K.C. Birendra, and K.J. Roux. 2015. Making the LINC: SUN and KASH protein
1062 interactions. *Biol Chem*. 396:295-310.
1063 Kural, C., A.S. Serpinskaya, Y.H. Chou, R.D. Goldman, V.I. Gelfand, and P.R. Selvin. 2007.
1064 Tracking melanosomes inside a cell to study molecular motors and their interaction.
1065 *Proc Natl Acad Sci U S A*. 104:5378-5382.
1066 Lavenus, S.B., S.M. Tudor, M.F. Ullo, K.W. Vosatka, and J.S. Logue. 2020. A flexible network of
1067 vimentin intermediate filaments promotes migration of amoeboid cancer cells
1068 through confined environments. *J Biol Chem*. 295:6700-6709.
1069 Leduc, C., and S. Etienne-Manneville. 2017. Regulation of microtubule-associated motors
1070 drives intermediate filament network polarization. *J Cell Biol*. 216:1689-1703.
1071 Lin, Y.C., C.P. Broedersz, A.C. Rowat, T. Wedig, H. Herrmann, F.C. Mackintosh, and D.A. Weitz.
1072 2010. Divalent cations crosslink vimentin intermediate filament tail domains to
1073 regulate network mechanics. *J Mol Biol*. 399:637-644.

1074 Lynch, C.D., A.M. Lazar, T. Iskratsch, X. Zhang, and M.P. Sheetz. 2013. Endoplasmic spreading
1075 requires coalescence of vimentin intermediate filaments at force-bearing adhesions.
1076 *Mol Biol Cell*. 24:21-30.
1077 Mahammad, S., S.N. Murthy, A. Didonna, B. Grin, E. Israeli, R. Perrot, P. Bomont, J.P. Julien, E.
1078 Kuczmarski, P. Opal, and R.D. Goldman. 2013. Giant axonal neuropathy-associated
1079 gigaxonin mutations impair intermediate filament protein degradation. *J Clin Invest*.
1080 123:1964-1975.
1081 Mavrakis, M., and M.A. Juanes. 2023. The compass to follow: Focal adhesion turnover. *Curr*
1082 *Opin Cell Biol*. 80:102152.
1083 Meiring, J.C.M., I. Grigoriev, W. Nijenhuis, L.C. Kapitein, and A. Akhmanova. 2022. Opto-
1084 katanin, an optogenetic tool for localized, microtubule disassembly. *Curr Biol*.
1085 32:4660-4674.
1086 Mendez, M.G., S.I. Kojima, and R.D. Goldman. 2010. Vimentin induces changes in cell shape,
1087 motility, and adhesion during the epithelial to mesenchymal transition. *FASEB J*.
1088 24:1838-1851.
1089 Mendez, M.G., D. Restle, and P.A. Janmey. 2014. Vimentin enhances cell elastic behavior and
1090 protects against compressive stress. *Biophys J*. 107:314-323.
1091 Messica, Y., A. Laser-Azogui, T. Volberg, Y. Elisha, K. Lysakovskaia, R. Eils, E. Gladilin, B. Geiger,
1092 and R. Beck. 2017. The role of Vimentin in Regulating Cell Invasive Migration in Dense
1093 Cultures of Breast Carcinoma Cells. *Nano Lett*. 17:6941-6948.
1094 Mohanasundaram, P., L.S. Coelho-Rato, M.K. Modi, M. Urbanska, F. Lautenschläger, F. Cheng,
1095 and J.E. Eriksson. 2022. Cytoskeletal vimentin regulates cell size and autophagy
1096 through mTORC1 signaling. *PLOS Biol*. 20:e3001737.
1097 Nekrasova, O.E., M.G. Mendez, I.S. Chernoivanenko, P.A. Tyurin-Kuzmin, E.R. Kuczmarski, V.I.
1098 Gelfand, R.D. Goldman, and A.A. Minin. 2011. Vimentin intermediate filaments
1099 modulate the motility of mitochondria. *Mol Biol Cell*. 22:2282-2289.
1100 Nery, F.C., J. Zeng, B.P. Niland, J. Hewett, J. Farley, D. Irimia, Y. Li, G. Wiche, A. Sonnenberg,
1101 and X.O. Breakefield. 2008. TorsinA binds the KASH domain of nesprins and
1102 participates in linkage between nuclear envelope and cytoskeleton. *J Cell Sci*.
1103 121:3476-3486.
1104 Nijenhuis, W., M.M.P.v. Grinsven, and L.C. Kapitein. 2020. An optimized toolbox for the
1105 optogenetic control of intracellular transport. *J Cell Biol*. 219:e201907149.
1106 Nishizawa, M., I. Izawa, A. Inoko, Y. Hayashi, K. Nagata, T. Yokoyama, J. Usukura, and M.
1107 Inagaki. 2005. Identification of trichoplein, a novel keratin filament-binding protein. *J*
1108 *Cell Sci*. 118:1081-1090.
1109 Nixon-Abell, J., C.J. Obara, A.V. Weigel, D. Li, W.R. Legant, C.S. Xu, H.A. Pasolli, K. Harvey, H.F.
1110 Hess, E. Betzig, C. Blackstone, and J. Lippincott-Schwartz. 2016. Increased
1111 spatiotemporal resolution reveals highly dynamic dense tubular matrices in the
1112 peripheral ER. *Science*. 354:aaf3928.
1113 Ostrowska-Podhorodecka, Z., I. Ding, M. Norouzi, and C.A. McCulloch. 2022. Impact of
1114 Vimentin on Regulation of Cell Signaling and Matrix Remodeling. *Front Cell Dev Biol*.
1115 10:869069.
1116 Özkan, N., M. Koppers, I. van Soest, A. van Harten, D. Jurriens, N. Liv, J. Klumperman, L.C.
1117 Kapitein, C.C. Hoogenraad, and G.G. Farías. 2021. ER – lysosome contacts at a pre-
1118 axonal region regulate axonal lysosome availability. *Nat Commun*. 12:4493.
1119 Paulin, D., A. Lilienbaum, S. Kardjian, O. Agbulut, and Z. Li. 2022. Vimentin: Regulation and
1120 pathogenesis. *Biochimie*. 197:96-112.

Petitjean, II, Q.D. Tran, A. Goutou, Z. Kabir, G. Wiche, C. Leduc, and G.H. Koenderink. 2024. Reconstitution of cytolinker-mediated crosstalk between actin and vimentin. *Eur J Cell Biol*. 103:151403.

Pogoda, K., and P.A. Janmey. 2023. Transmit and protect: The mechanical functions of intermediate filaments. *Curr Opin Cell Biol*. 85:102281.

Pollock, R., R. Issner, K. Zoller, S. Natesan, V.M. Rivera, and T. Clackson. 2000. Delivery of a stringent dimerizer-regulated gene expression system in a single retroviral vector. *Proc Natl Acad Sci U S A*. 97:13221-13226.

Prahlad, V., M. Yoon, R.D. Moir, R.D. Vale, and R.D. Goldman. 1998. Rapid movements of vimentin on microtubule tracks: Kinesin-dependent assembly of intermediate filament networks. *J Cell Biol*. 143:159-170.

Reed, N.A., D. Cai, T.L. Blasius, G.T. Jih, E. Meyhofer, J. Gaertig, and K.J. Verhey. 2006. Microtubule acetylation promotes kinesin-1 binding and transport. *Curr Biol*. 16:2166-2172.

Ridge, K.M., D. Shumaker, A. Robert, C. Hookway, V.I. Gelfand, P.A. Janmey, J. Lowery, M. Guo, D.A. Weitz, E. Kuczmarski, and R.D. Goldman. 2016. Methods for Determining the Cellular Functions of Vimentin Intermediate Filaments. *Methods Enzymol*. 568:389-426.

Robert, A., P. Tian, S.A. Adam, M. Kittisopikul, K. Jaqaman, R.D. Goldman, and V.I. Gelfand. 2019. Kinesin-dependent transport of keratin filaments: a unified mechanism for intermediate filament transport. *FASEB J*. 33:388-399.

Saldanha, R., M.T.H. Thanh, N. Krishnan, H. Hehnly, and A.E. Patteson. 2023. Vimentin supports cell polarization by enhancing centrosome function and microtubule acetylation. *bioRxiv*:2023.2002.2017.528977.

Schaedel, L., C. Lorenz, A.V. Schepers, S. Klumpp, and S. Köster. 2021. Vimentin intermediate filaments stabilize dynamic microtubules by direct interactions. *Nat Commun*. 12:3799.

Schwarz, N., R. Windoffer, T.M. Magin, and R.E. Leube. 2015. Dissection of keratin network formation, turnover and reorganization in living murine embryos. *Sci Rep*. 5:9007.

Sha, Y., D. Haensel, G. Gutierrez, H. Du, X. Dai, Q. Nie, Y. Sha, D. Haensel, G. Gutierrez, H. Du, X. Dai, and Q. Nie. 2019. Intermediate cell states in epithelial-to-mesenchymal transition. *Phys Biol*. 16:021001.

Shaebani, M.R., L. Stankevicins, D. Vesperini, M. Urbanska, D.A.D. Flormann, E. Terriac, A.K.B. Gad, F. Cheng, J.E. Eriksson, and F. Lautenschläger. 2022. Effects of vimentin on the migration, search efficiency, and mechanical resilience of dendritic cells. *Biophys J*. 121:3950-3961.

Smal, I., K. Draegestein, N. Galjart, W. Niessen, and E. Meijering. 2008. Particle filtering for multiple object tracking in dynamic fluorescence microscopy images: application to microtubule growth analysis. *IEEE Trans Med Imaging*. 27:789-804.

Strelkov, S.V., H. Herrmann, N. Geisler, T. Wedig, R. Zimbelmann, U. Aebi, and P. Burkhard. 2002. Conserved segments 1A and 2B of the intermediate filament dimer: their atomic structures and role in filament assembly. *EMBO J*. 21:1255-1266.

Swoger, M., S. Gupta, E.E. Charrier, M. Bates, H. Hehnly, and A.E. Patteson. 2022. Vimentin Intermediate Filaments Mediate Cell Morphology on Viscoelastic Substrates. *ACS Appl Bio Mater*. 5:552-561.

1166 Trogden, K.P., R.A. Battaglia, P. Kabiraj, V.J. Madden, H. Herrmann, and N.T. Snider. 2018. An
1167 image-based small-molecule screen identifies vimentin as a pharmacologically
1168 relevant target of simvastatin in cancer cells. *FASEB J*. 32:2841-2854.
1169 Tsuruta, D., and J.C.R. Jones. 2003. The vimentin cytoskeleton regulates focal contact size
1170 and adhesion of endothelial cells subjected to shear stress. *J Cell Sci*. 116:4977-4984.
1171 Usman, S., H. Aldehlawi, T.K.N. Nguyen, M.T. Teh, and A. Waseem. 2022. Impact of N-
1172 Terminal Tags on De Novo Vimentin Intermediate Filament Assembly. *Int J Mol Sci*.
1173 23: 6349.
1174 Velez-delValle, C., M. Marsch-Moreno, F. Castro-Munozledo, I.J. Galvan-Mendoza, and W.
1175 Kuri-Harcuch. 2016. Epithelial cell migration requires the interaction between the
1176 vimentin and keratin intermediate filaments. *Sci Rep*. 6:24389.
1177 Venu, A.P., M. Modi, U. Aryal, E. Tcarenkova, Y. Jiu, G. Jacquemet, A. Minin, F. Cheng, and J.E.
1178 Eriksson. 2022. Vimentin supports directional cell migration by controlling focal
1179 adhesions. *bioRxiv*:2022.2010.2002.510295.
1180 Wiche, G., and M.A. Baker. 1982. Cytoplasmic network arrays demonstrated by
1181 immunolocalization using antibodies to a high molecular weight protein present in
1182 cytoskeletal preparations from cultured cells. *Exp Cell Res*. 138:15-29.
1183 Wiche, G., and L. Winter. 2011. Plectin isoforms as organizers of intermediate filament
1184 cytoarchitecture. *Bioarchitecture*. 1:14-20.
1185 Zhu, W., A. Cowie, G.W. Wasfy, L.Z. Penn, B. Leber, and D.W. Andrews. 1996. Bcl-2 mutants
1186 with restricted subcellular location reveal spatially distinct pathways for apoptosis in
1187 different cell types. *EMBO J*. 15:4130-4141.

Figure 1

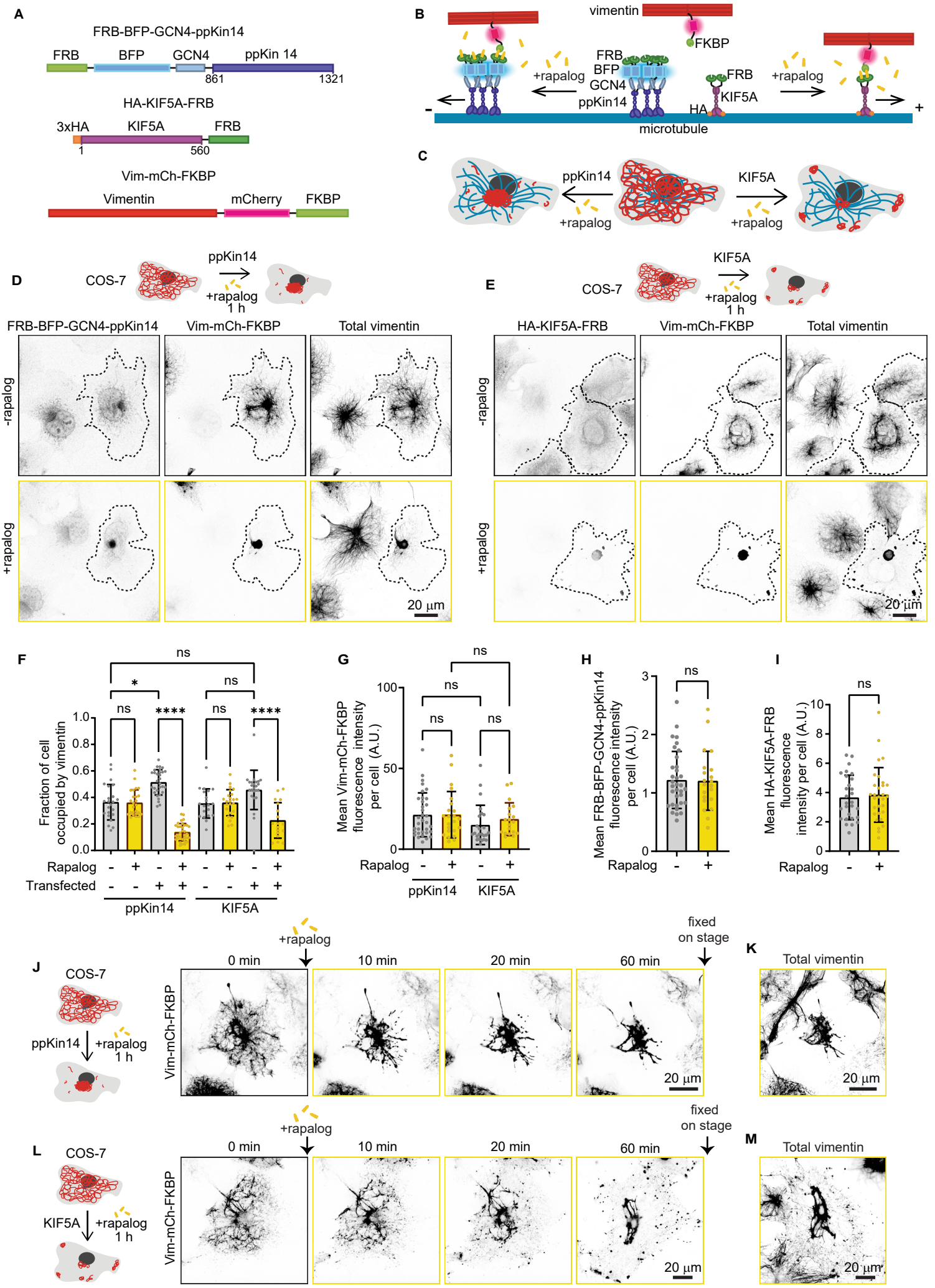
A
FRB-BFP-GCN4-ppKin14
FRB
BFP
GCN4
ppKin 14
861
1321
HA-KIF5A-FRB
3xHA
KIF5A
FRB
1
560
Vim-mCh-FKBP
Vimentin
mCherry
FKBP
B
vimentin
FKBP
FRB
BFP
GCN4
ppKin14
+rapalog
FRB
KIF5A
HA
+rapalog
-
+
microtubule
C
ppKin14
+rapalog
KIF5A
+rapalog
D
COS-7
ppKin14
+rapalog
1 h
FRB-BFP-GCN4-ppKin14
Vim-mCh-FKBP
Total vimentin
-rapalog
+rapalog
20 µm
E
COS-7
KIF5A
+rapalog
1 h
HA-KIF5A-FRB
Vim-mCh-FKBP
Total vimentin
-rapalog
+rapalog
20 µm
F
Fraction of cell occupied by vimentin
ns
*
ns
ns
****
ns
****
Rapalog
Transfected
ppKin14
KIF5A
G
Mean Vim-mCh-FKBP fluorescence intensity per cell (A.U.)
ns
ns
ns
ns
Rapalog
ppKin14
KIF5A
H
Mean FRB-BFP-GCN4-ppKin14 fluorescence intensity per cell (A.U.)
ns
Rapalog
I
Mean HA-KIF5A-FRB fluorescence intensity per cell (A.U.)
ns
Rapalog
J
COS-7
ppKin14
+rapalog
1 h
+rapalog
fixed on stage
0 min
10 min
20 min
60 min
Vim-mCh-FKBP
20 µm
K
Total vimentin
20 µm
L
COS-7
KIF5A
+rapalog
1 h
+rapalog
fixed on stage
0 min
10 min
20 min
60 min
Vim-mCh-FKBP
20 µm
M
Total vimentin
20 µm

Figure 2

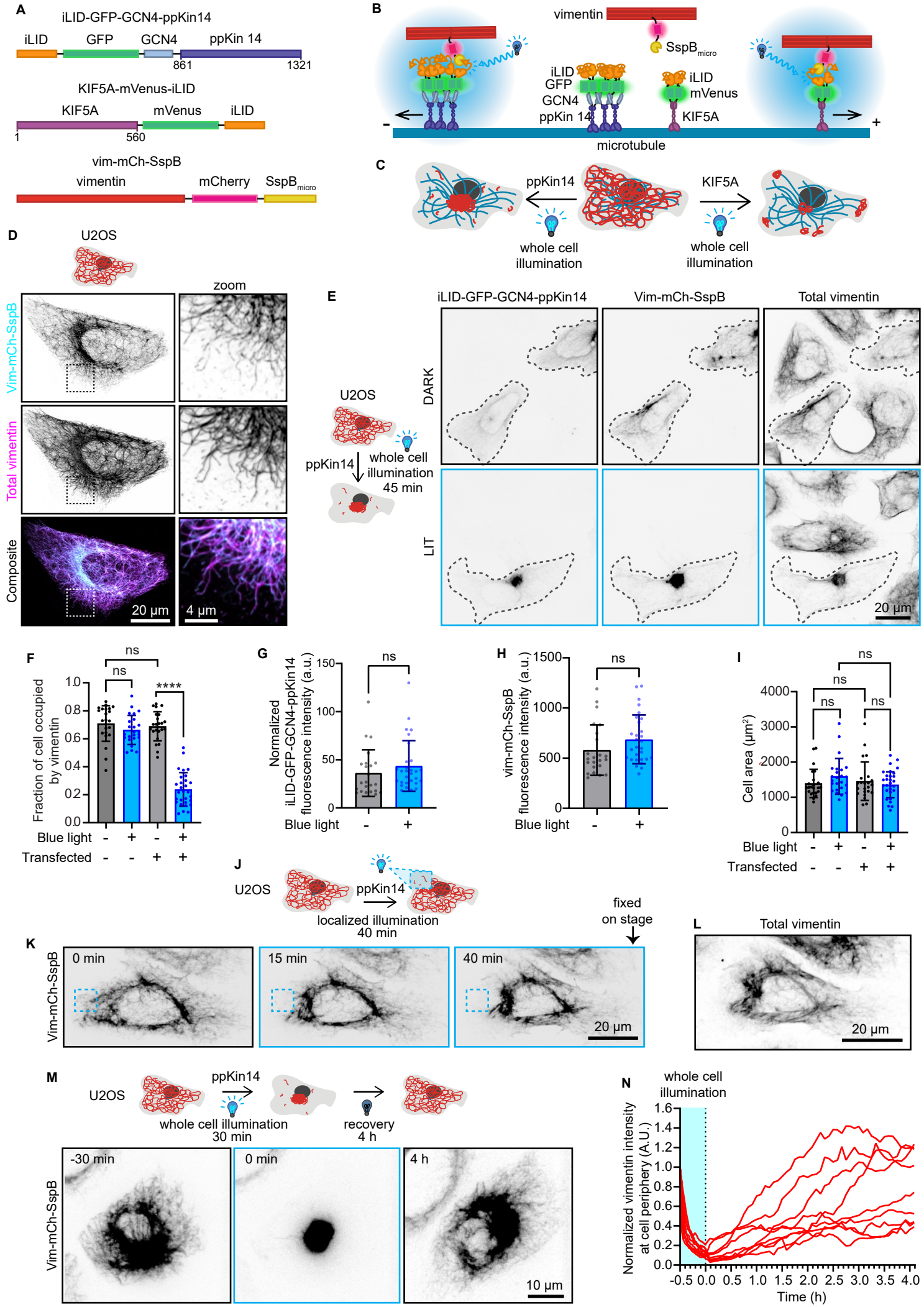
A
iLID-GFP-GCN4-ppKin14
iLID
GFP
GCN4
ppKin 14
861
1321
KIF5A-mVenus-iLID
KIF5A
mVenus
iLID
1
560
vim-mCh-SspB
vimentin
mCherry
SspB micro
B
vimentin
SspB micro
iLID
GFP
GCN4
ppKin 14
iLID
mVenus
KIF5A
microtubule
C
ppKin14
KIF5A
whole cell illumination
whole cell illumination
D
U2OS
zoom
Vim-mCh-SspB
Total vimentin
Composite
20 µm
4 µm
E
iLID-GFP-GCN4-ppKin14
Vim-mCh-SspB
Total vimentin
U2OS
ppKin14
whole cell illumination 45 min
DARK
LIT
20 µm
F
Fraction of cell occupied by vimentin
ns
ns
****
Blue light
Transfected
G
Normalized iLID-GFP-GCN4-ppKin14 fluorescence intensity (a.u.)
ns
Blue light
H
vim-mCh-SspB fluorescence intensity (a.u.)
ns
Blue light
I
Cell area (µm²)
ns
ns
ns
ns
Blue light
Transfected
J
U2OS
ppKin14
localized illumination 40 min
fixed on stage
K
Vim-mCh-SspB
0 min
15 min
40 min
20 µm
L
Total vimentin
20 µm
M
U2OS
ppKin14
whole cell illumination 30 min
recovery 4 h
Vim-mCh-SspB
-30 min
0 min
4 h
10 µm
N
whole cell illumination
Normalized vimentin intensity at cell periphery (A.U.)
Time (h)

Figure 3

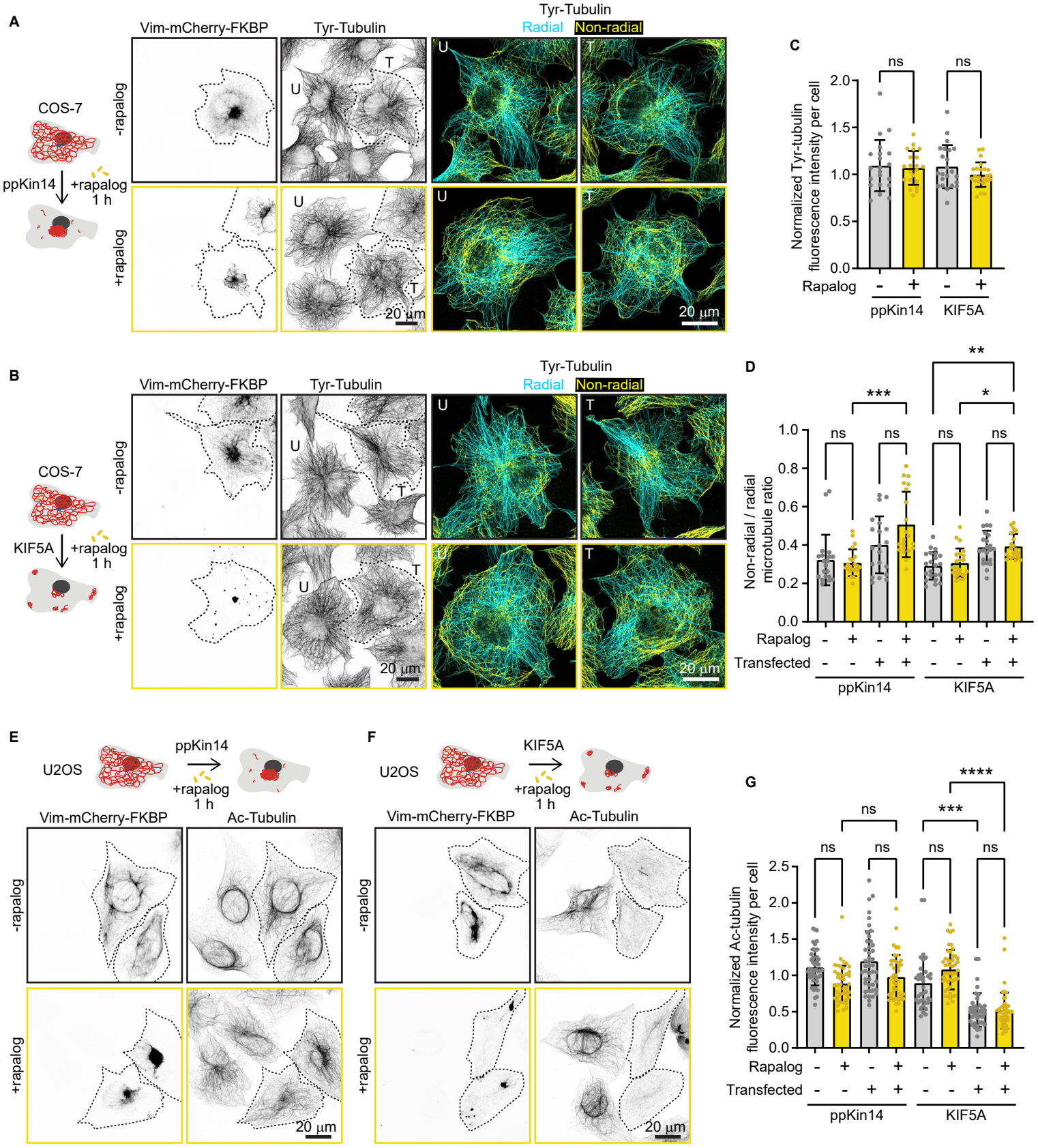
A
Vim-mCherry-FKBP
Tyr-Tubulin
Tyr-Tubulin
Radial
Non-radial
COS-7
ppKin14
+rapalog
1 h
-rapalog
+rapalog
U
T
20 µm
B
KIF5A
C
Normalized Tyr-tubulin fluorescence intensity per cell
ns
Rapalog
ppKin14
KIF5A
D
Non-radial / radial microtubule ratio
Transfected
E
U2OS
Ac-Tubulin
F
G
Normalized Ac-tubulin fluorescence intensity per cell
****
***
**
*

Figure 4

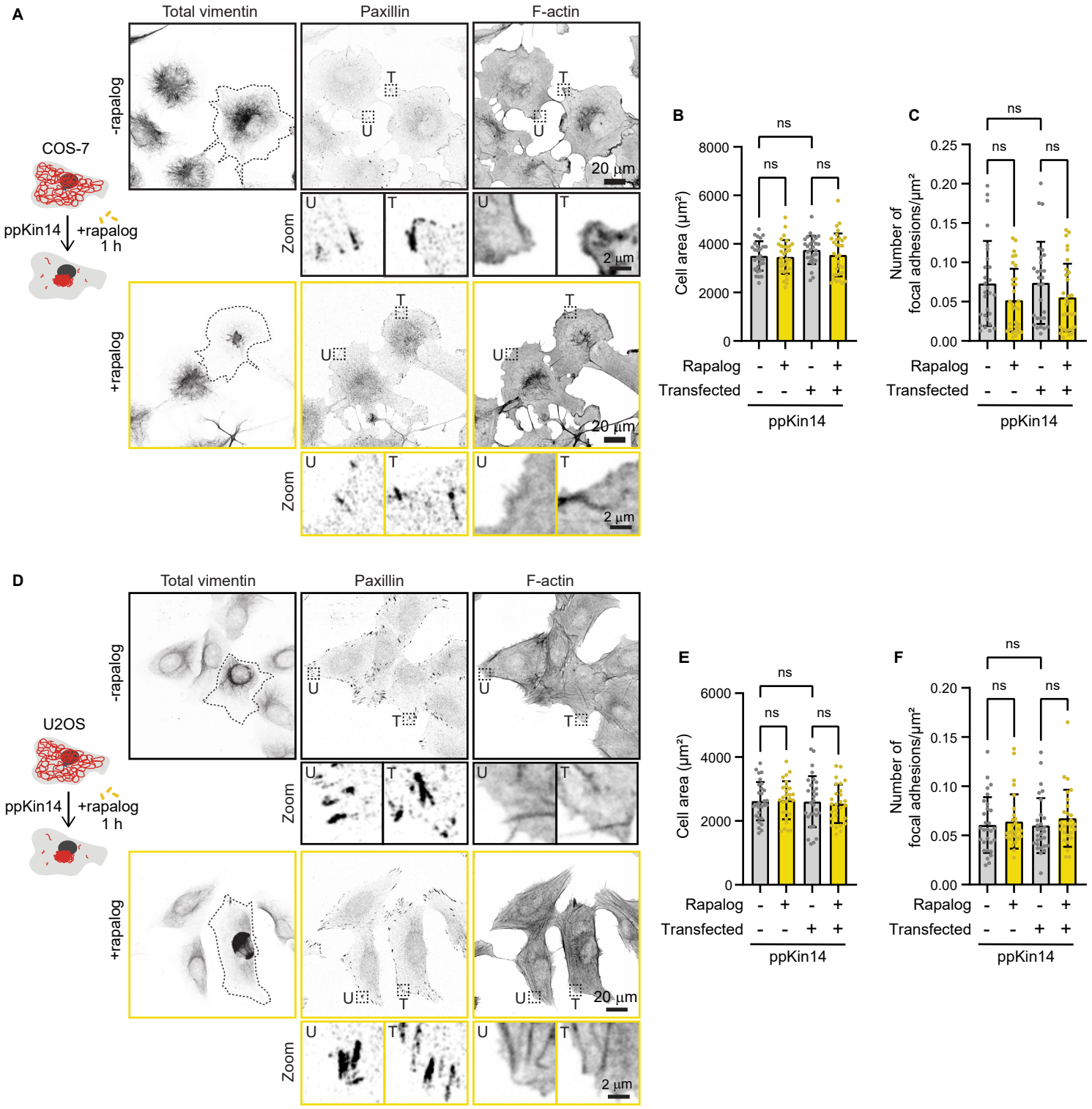
A
Total vimentin
Paxillin
F-actin
-rapalog
+rapalog
COS-7
ppKin14
+rapalog
1 h
Zoom
T
U
20 µm
2 µm
B
C
ns
Cell area (µm²)
Number of focal adhesions/µm²
Rapalog
Transfected
ppKin14
D
U2OS
E
F

Figure 5

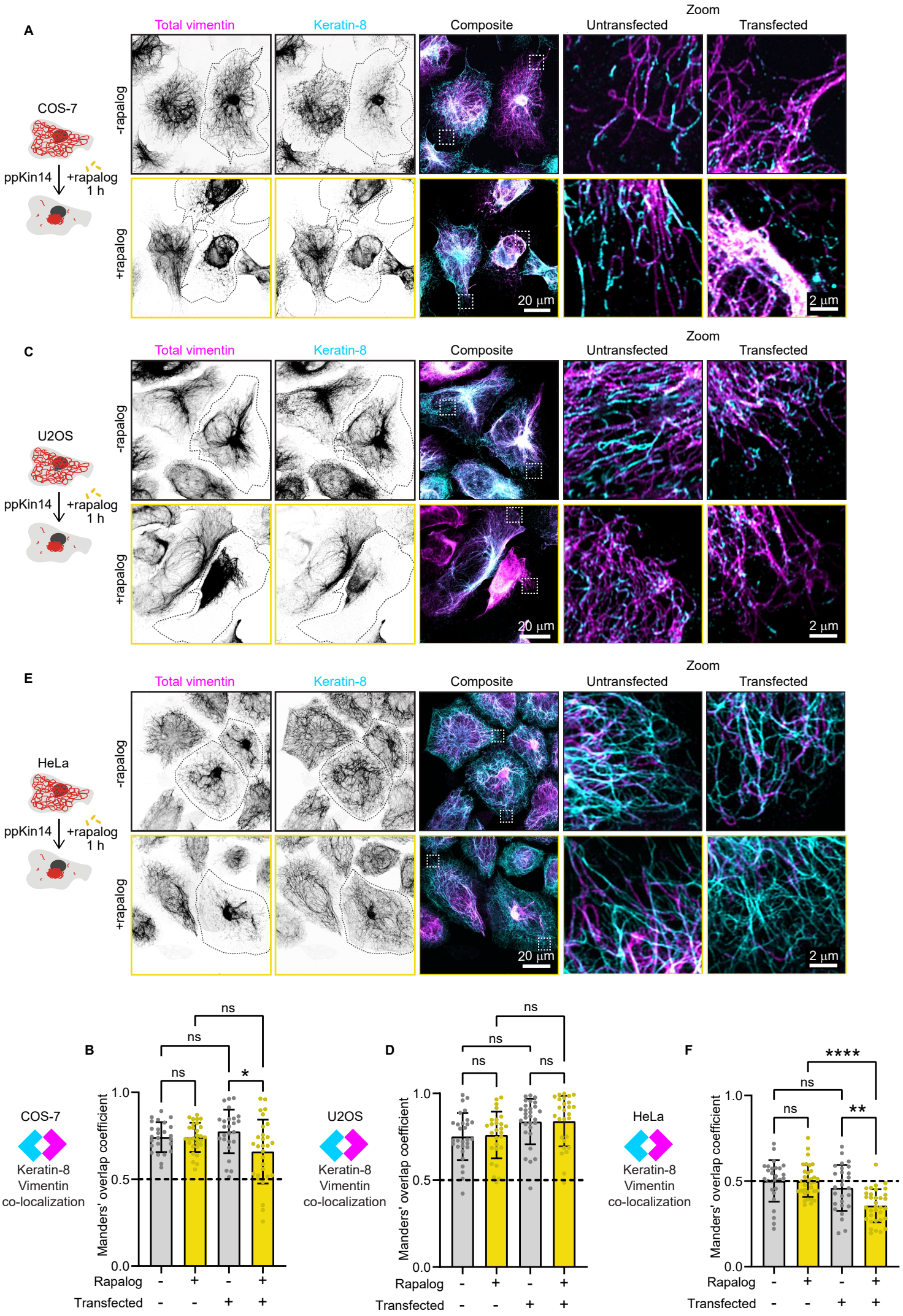
A
COS-7
ppKin14
+rapalog
1 h
-rapalog
+rapalog
Total vimentin
Keratin-8
Composite
Zoom
Untransfected
Transfected
20 µm
2 µm
C
U2OS
E
HeLa
B
COS-7
Keratin-8
Vimentin
co-localization
Manders' overlap coefficient
1.0
0.5
0.0
ns
*
Rapalog
Transfected
D
U2OS
F
HeLa
****
**

Figure 6

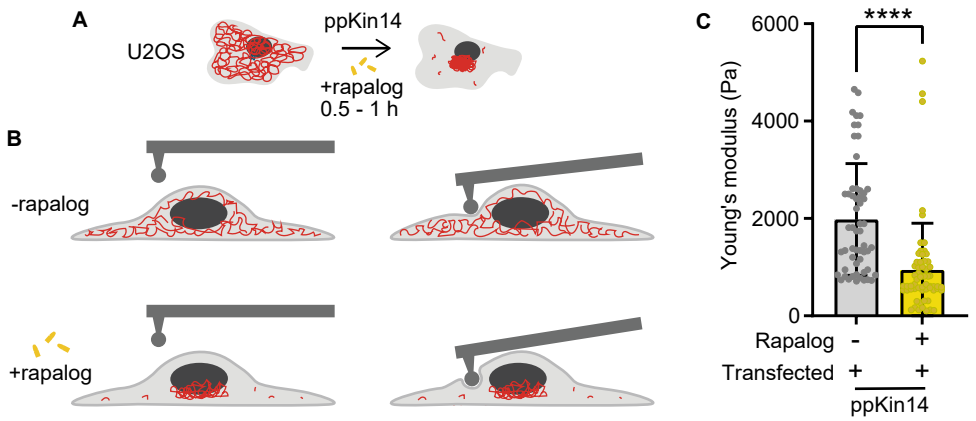
A
U2OS
ppKin14
+rapalog
0.5 - 1 h
B
-rapalog
+rapalog
C
****
Young's modulus (Pa)
6000
4000
2000
0
Rapalog - +
Transfected + +
ppKin14

Figure 7

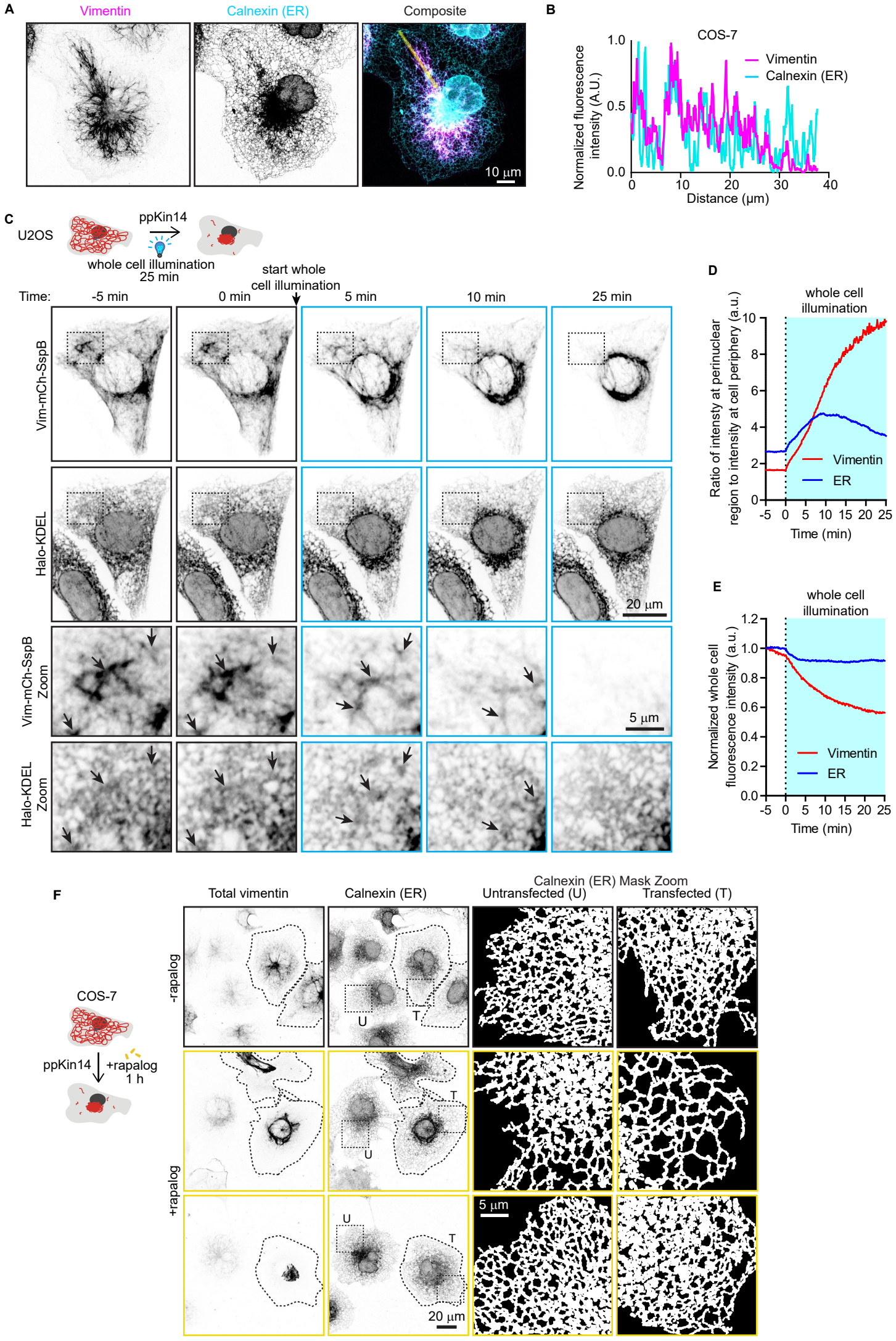
A
Vimentin
Calnexin (ER)
Composite
10 µm
B
COS-7
Vimentin
Calnexin (ER)
Normalized fluorescence intensity (A.U.)
1.0
0.5
0.0
0
10
20
30
40
Distance (µm)
C
U2OS
ppKin14
whole cell illumination
25 min
start whole cell illumination
Time:
-5 min
0 min
5 min
10 min
25 min
Vim-mCh-SspB
Halo-KDEL
20 µm
Vim-mCh-SspB Zoom
Halo-KDEL Zoom
5 µm
D
whole cell illumination
Ratio of intensity at perinuclear region to intensity at cell periphery (a.u.)
Vimentin
ER
Time (min)
E
whole cell illumination
Normalized whole cell fluorescence intensity (a.u.)
Vimentin
ER
Time (min)
F
Total vimentin
Calnexin (ER)
Calnexin (ER) Mask Zoom
Untransfected (U)
Transfected (T)
COS-7
ppKin14
+rapalog
1 h
-rapalog
+rapalog
U
T
5 µm
20 µm

Figure 8

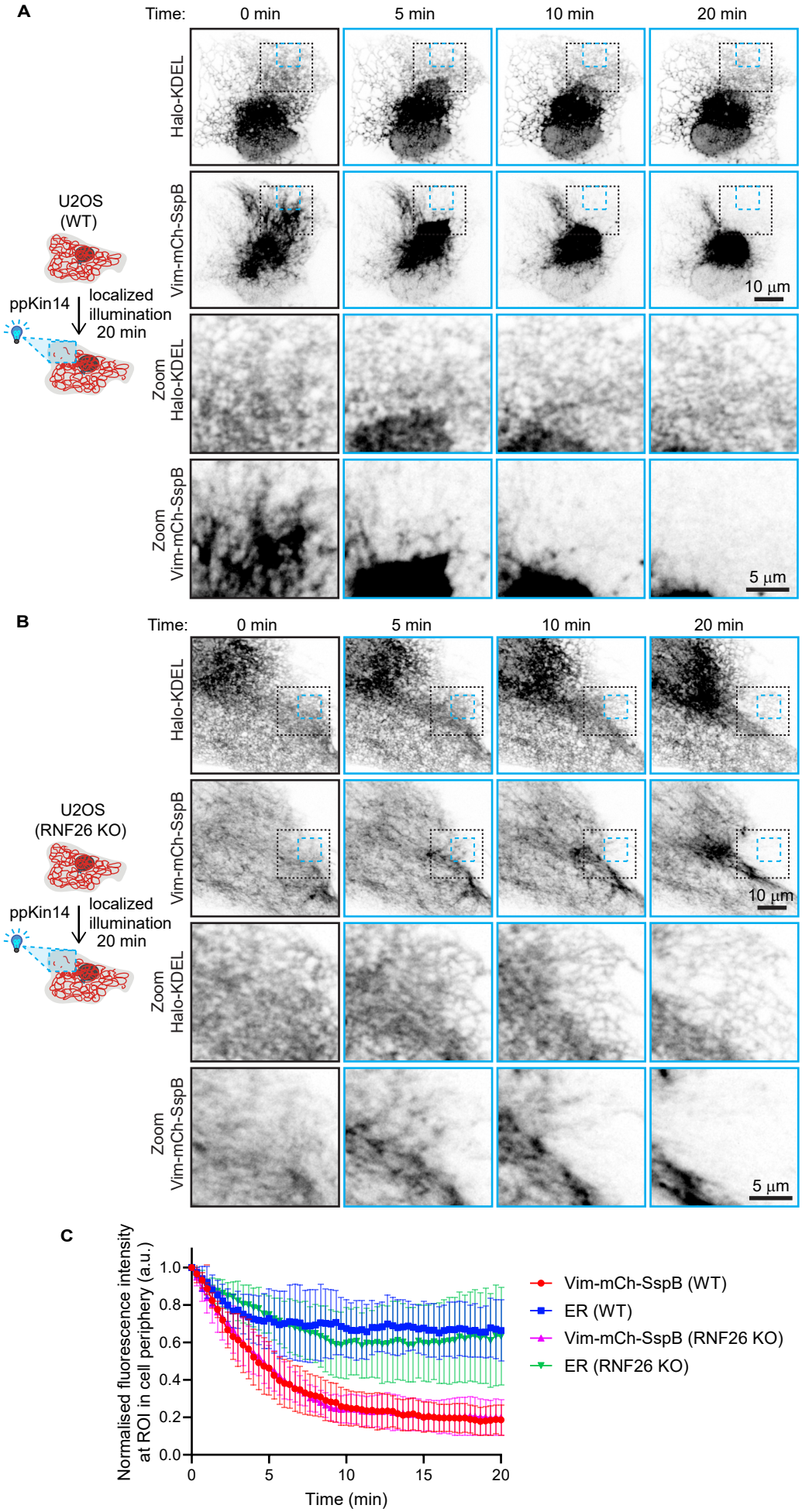
A
Time:
0 min
5 min
10 min
20 min
Halo-KDEL
Vim-mCh-SspB
Zoom Halo-KDEL
Zoom Vim-mCh-SspB
U2OS (WT)
ppKin14
localized illumination 20 min
10 µm
5 µm
B
U2OS (RNF26 KO)
C
Normalised fluorescence intensity at ROI in cell periphery (a.u.)
Time (min)
Vim-mCh-SspB (WT)
ER (WT)
Vim-mCh-SspB (RNF26 KO)
ER (RNF26 KO)

Figure 9

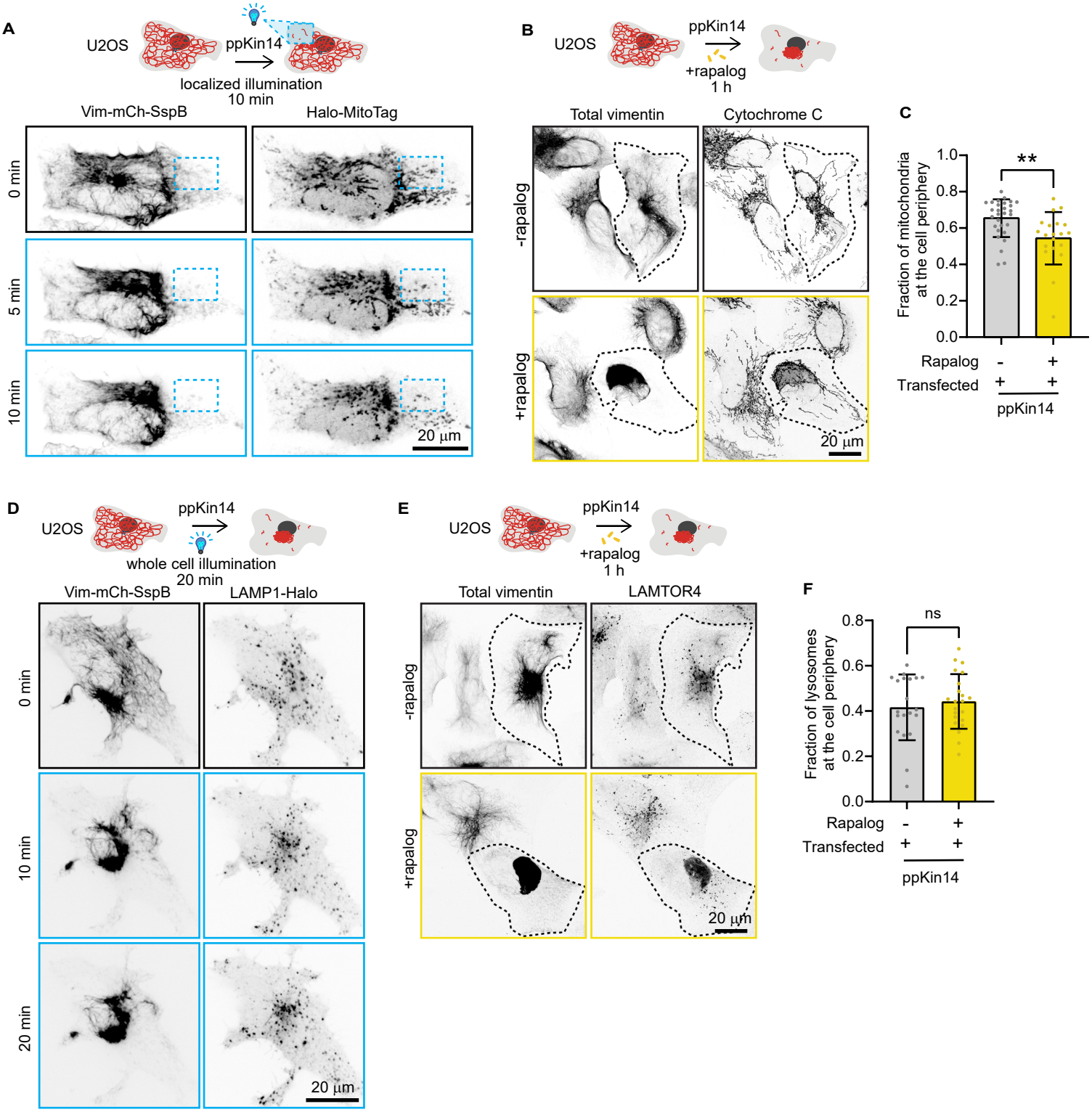
A
U2OS
ppKin14
localized illumination
10 min
Vim-mCh-SspB
Halo-MitoTag
0 min
5 min
10 min
20 µm
B
U2OS
ppKin14
+rapalog
1 h
Total vimentin
Cytochrome C
-rapalog
+rapalog
20 µm
C
Fraction of mitochondria at the cell periphery
1.0
0.8
0.6
0.4
0.2
0.0
**
Rapalog - +
Transfected + +
ppKin14
D
U2OS
ppKin14
whole cell illumination
20 min
Vim-mCh-SspB
LAMP1-Halo
0 min
10 min
20 min
20 µm
E
U2OS
ppKin14
+rapalog
1 h
Total vimentin
LAMTOR4
-rapalog
+rapalog
20 µm
F
Fraction of lysosomes at the cell periphery
0.8
0.6
0.4
0.2
0.0
ns
Rapalog - +
Transfected + +
ppKin14

Figure S1

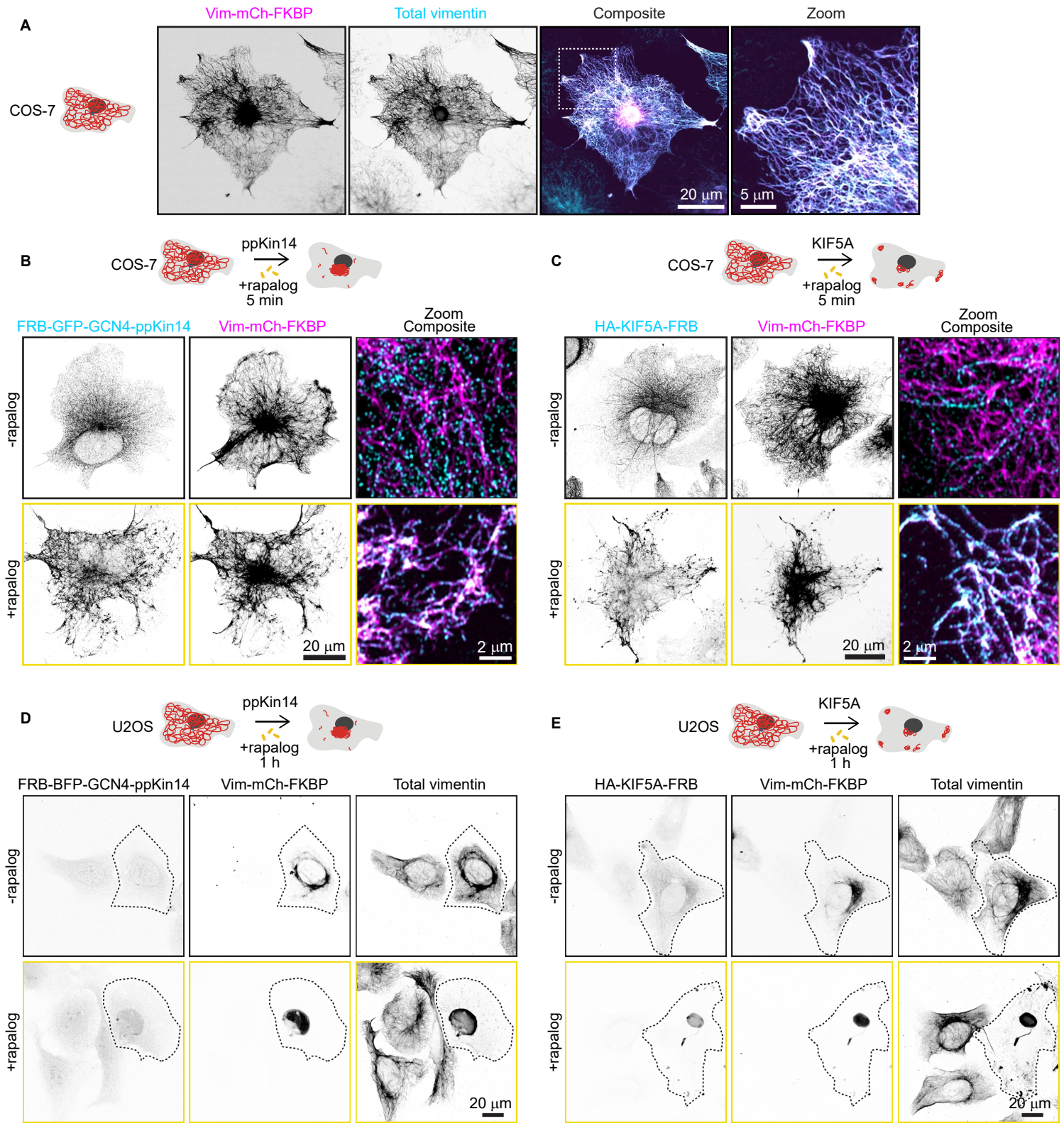
A
COS-7
Vim-mCh-FKBP
Total vimentin
Composite
Zoom
20 µm
5 µm
B
COS-7
ppKin14
+rapalog
5 min
FRB-GFP-GCN4-ppKin14
Vim-mCh-FKBP
Zoom
Composite
-rapalog
+rapalog
20 µm
2 µm
C
COS-7
KIF5A
+rapalog
5 min
HA-KIF5A-FRB
Vim-mCh-FKBP
Zoom
Composite
-rapalog
+rapalog
20 µm
2 µm
D
U2OS
ppKin14
+rapalog
1 h
FRB-BFP-GCN4-ppKin14
Vim-mCh-FKBP
Total vimentin
-rapalog
+rapalog
20 µm
E
U2OS
KIF5A
+rapalog
1 h
HA-KIF5A-FRB
Vim-mCh-FKBP
Total vimentin
-rapalog
+rapalog
20 µm

Figure S2

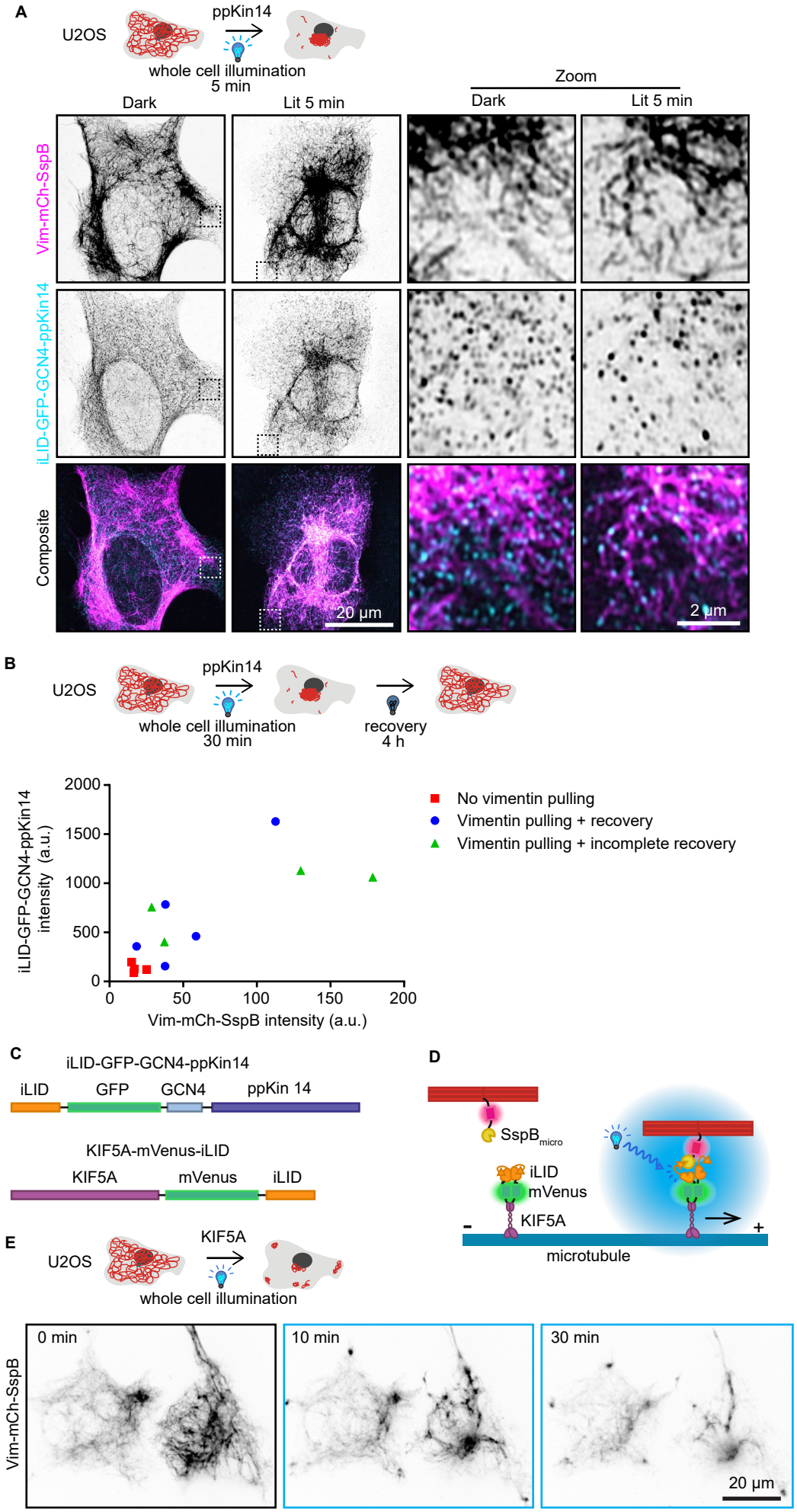
A
U2OS
ppKin14
whole cell illumination
5 min
Dark
Lit 5 min
Zoom
Dark
Lit 5 min
Vim-mCh-SspB
iLID-GFP-GCN4-ppKin14
Composite
20 µm
2 µm
B
U2OS
ppKin14
whole cell illumination
30 min
recovery
4 h
iLID-GFP-GCN4-ppKin14 intensity (a.u.)
Vim-mCh-SspB intensity (a.u.)
No vimentin pulling
Vimentin pulling + recovery
Vimentin pulling + incomplete recovery
C
iLID-GFP-GCN4-ppKin14
iLID
GFP
GCN4
ppKin 14
KIF5A-mVenus-iLID
KIF5A
mVenus
iLID
D
SspB micro
iLID
mVenus
KIF5A
microtubule
E
U2OS
KIF5A
whole cell illumination
Vim-mCh-SspB
0 min
10 min
30 min
20 µm

Figure S3

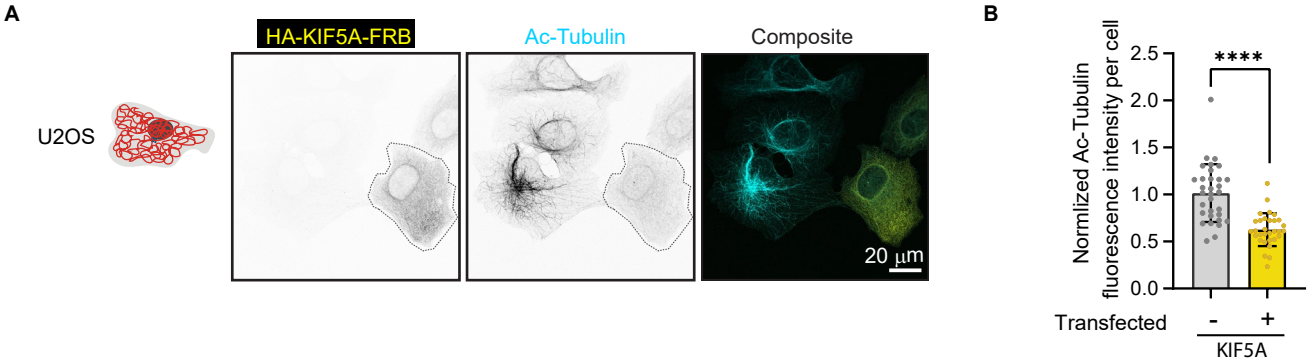
A
HA-KIF5A-FRB
Ac-Tubulin
Composite
U2OS
20 µm
B
Normlized Ac-Tubulin fluorescence intensity per cell
2.5
2.0
1.5
1.0
0.5
0.0
****
Transfected
-
+
KIF5A

Figure S4

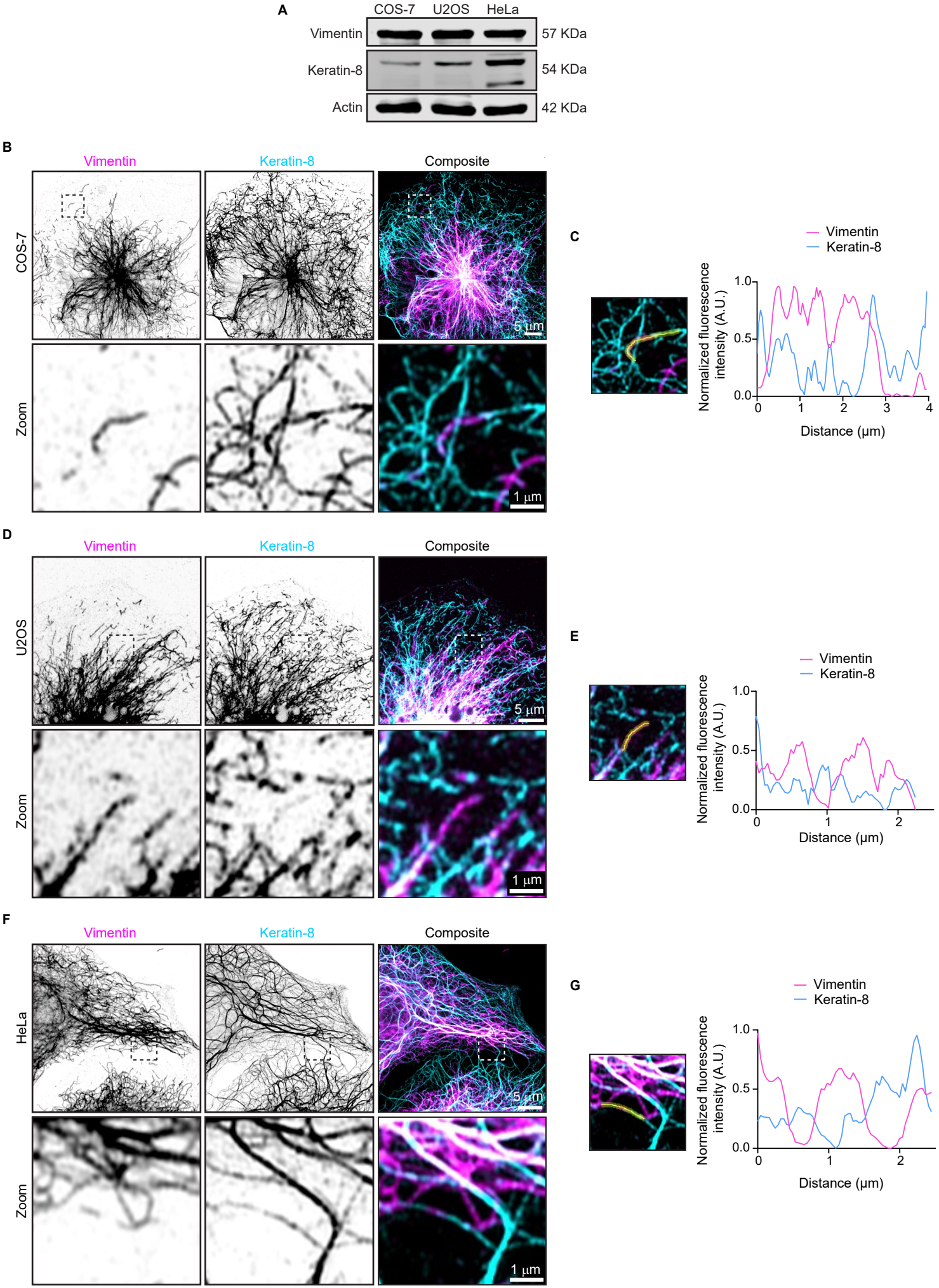
A
COS-7
U2OS
HeLa
Vimentin
Keratin-8
Actin
57 KDa
54 KDa
42 KDa
B
Vimentin
Keratin-8
Composite
COS-7
Zoom
5 µm
1 µm
C
Vimentin
Keratin-8
Normalized fluorescence intensity (A.U.)
Distance (µm)
D
U2OS
E
F
HeLa
G

Figure S5

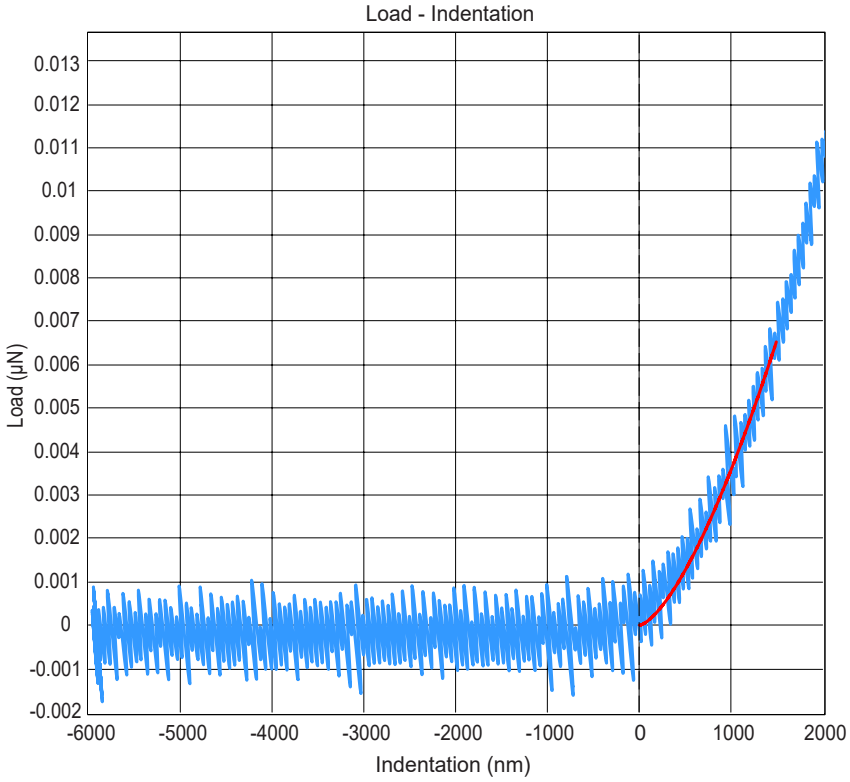
Load - Indentation
Load (µN)
0.013
0.012
0.011
0.01
0.009
0.008
0.007
0.006
0.005
0.004
0.003
0.002
0.001
0
-0.001
-0.002
-6000
-5000
-4000
-3000
-2000
-1000
0
1000
2000
Indentation (nm)
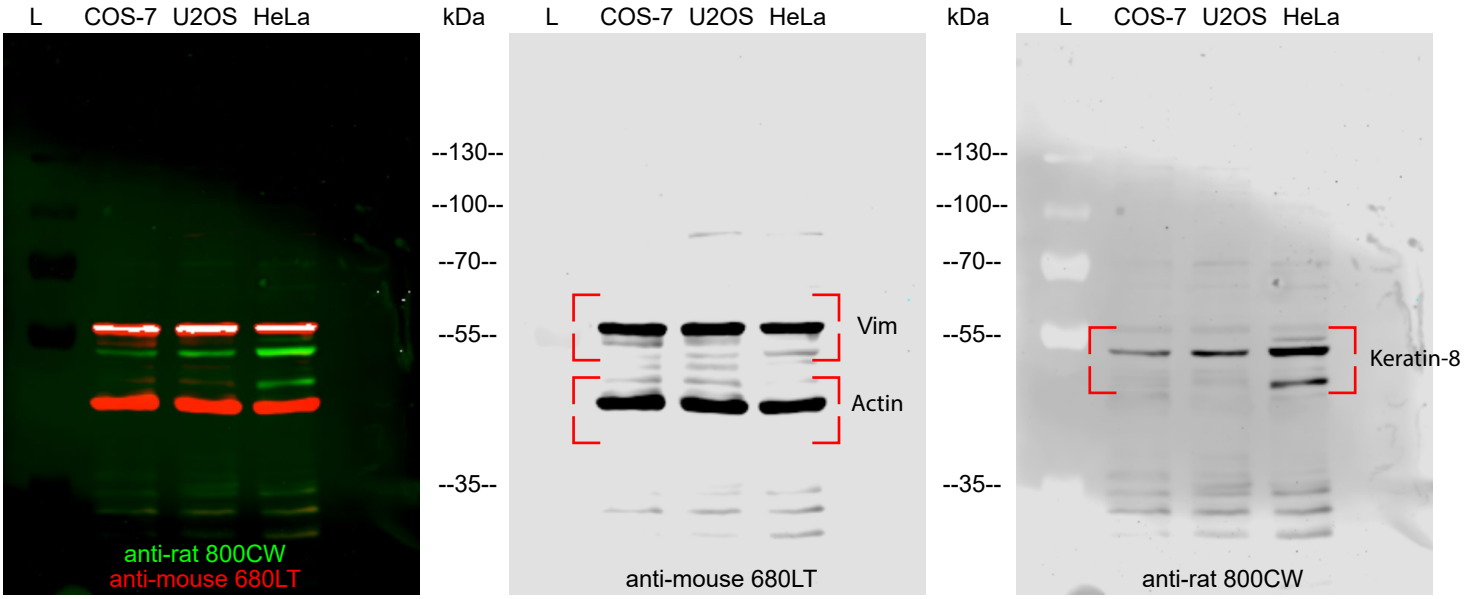
Source Data Figure S4